JGR Oceans

RESEARCH ARTICLE

10.1029/2025JC023848

Contrasting Responses of Dissolved Oxygen in the Northern Benguela Upwelling System to Four Decades of Warming

Amr Talaat Salama[1], **Elisa Lovecchio**[2], **Tomas Lovato**[1], **Momme Butenschön**[1], **Marco Zavatarelli**[3], **and Stephanie Henson**[2]

[1]CMCC Foundation - Euro-Mediterranean Center on Climate Change, Bologna, Italy, [2]National Oceanography Centre, Southampton, UK, [3]Department of Physics and Astronomy, Alma Mater Studiorum Università di Bologna, Bologna, Italy

Abstract The Northern Benguela Upwelling System (NBUS) is a highly productive yet low-oxygen region, influenced by the combined effects of circulation and biogeochemical processes. Using data from a high-resolution (~7 km) coupled physical–biogeochemical model spanning 1980–2020, this study investigates long-term dissolved oxygen (DO) variability in the NBUS. Model results show a total DO loss of ~1 Tmol in the upper 1,000 m, with a pronounced vertical dipole: the upper 400 m experienced net oxygenation (0.3 Tmol), while the 400–1,000 m layer accounted for significant depletion (1.3 Tmol). Oxygenation in upper layers is linked to enhanced turbulence due to intensified alongshore wind stress, as well as reduced intrusion of oxygen-poor South Atlantic Central Water. In contrast, deoxygenation at depth is primarily associated with increasing ocean heat content (OHC) and vertical stratification, with the OHC increase likely linked to changes in intermediate waters entering the domain. Divergent changes in the oxygen minimum zone (OMZ) include contraction of OMZ_{20} (waters with DO < 20 mmol m^{-3}) and deepening of OMZ_{60} (DO < 60 mmol m^{-3}) and OMZ_{120} (DO < 120 mmol m^{-3}) by approximately 120 m. The deepening of OMZ_{60} and OMZ_{120}, along with bottom water deoxygenation, poses major ecological concerns in the NBUS. Low-oxygen-tolerant pelagic fish are especially at risk, potentially reducing fishery yields. Declining oxygen also threatens benthic biodiversity by eliminating sensitive species and favoring low-oxygen-adapted ones.

Plain Language Summary The Northern Benguela Upwelling System off southwest Africa is one of the world's most productive marine regions, but it naturally contains very low oxygen levels. Using the data from a high-resolution ocean model covering the last 4 decades (1980–2020), we examined how oxygen in this region has changed and why. We found a clear two-layer response: the upper ocean has gained oxygen, mainly because stronger winds have increased mixing and ventilation, while deeper waters have lost oxygen due to warming, partly linked to changes in the water masses entering the region, and increasing stratification that limits the supply of oxygen from above. These changes are reshaping the region's oxygen-poor zones. The shallowest, most extreme low-oxygen waters are shrinking, but a much larger and deeper low-oxygen layer is expanding. This expansion threatens fish species that rely on deep habitats. Our results highlight the importance of both circulation-driven ocean warming and changes in wind patterns in controlling oxygen availability in the Northern Benguela system.

Key Points:

- Upper waters in the Northern Benguela oxygenate via wind-induced mixing, while deeper layers deoxygenate under water-mass-linked warming
- Causality analysis shows depth-varying DO links: winds and mixing dominate above 400 m, while stratification and warming dominate below
- Oxygen minimum zones of 20 mmol m^{-3} contract, while zones of 60 and 120 mmol m^{-3} deepen, with potential negative impacts on deep habitats

Supporting Information:

Supporting Information may be found in the online version of this article.

Correspondence to:

A. T. Salama,
amr.salama@cmcc.it

Citation:

Salama, A. T., Lovecchio, E., Lovato, T., Butenschön, M., Zavatarelli, M., & Henson, S. (2026). Contrasting responses of dissolved oxygen in the Northern Benguela Upwelling System to four decades of warming. *Journal of Geophysical Research: Oceans*, *131*, e2025JC023848. https://doi.org/10.1029/2025JC023848

Received 29 NOV 2025
Accepted 15 JUN 2026

Author Contributions:

Conceptualization: Amr Talaat Salama, Elisa Lovecchio, Tomas Lovato, Momme Butenschön, Marco Zavatarelli, Stephanie Henson
Data curation: Amr Talaat Salama, Tomas Lovato
Methodology: Amr Talaat Salama, Elisa Lovecchio, Tomas Lovato
Validation: Amr Talaat Salama, Elisa Lovecchio, Tomas Lovato
Visualization: Amr Talaat Salama, Elisa Lovecchio
Writing – original draft: Amr Talaat Salama

1. Introduction

Dissolved oxygen (DO) inventory in the global ocean has declined by approximately 2% since the 1960s (Schmidtko et al., 2017), largely as a consequence of anthropogenic climate warming (Hollitzer et al., 2024). The most recent CMIP6-based projections estimate a subsurface (100–600 m) oxygen decline of −4.1% ± 4.2% by 2100 under the most optimistic scenario (SSP1-2.6), with greater losses projected under higher-emission pathways (Cooley et al., 2022; Kwiatkowski et al., 2020). This deoxygenation is particularly pronounced in coastal oceans (Gilbert et al., 2010; Pitcher et al., 2021). Such DO loss poses serious implications, as DO is essential for sustaining marine life and regulating major oceanic elemental cycles (Breitburg et al., 2018). Among the most affected regions are the Eastern Boundary Upwelling Systems, which are characterized by high ecosystem productivity and support some of the world's most important fisheries (García-Reyes et al., 2015; Garçon et al., 2019; Kainge et al., 2020).

The Benguela Upwelling System (BUS), located along the southwest African coast (Figure 1a), is one of the most productive marine ecosystems globally (Carr, 2001; Messié et al., 2009). This productivity is sustained by wind-induced upwelling, where alongshore winds, combined with the Coriolis effect, advect surface waters offshore,

Writing – review & editing: Amr Talaat Salama, Elisa Lovecchio, Tomas Lovato, Momme Butenschön, Marco Zavatarelli, Stephanie Henson

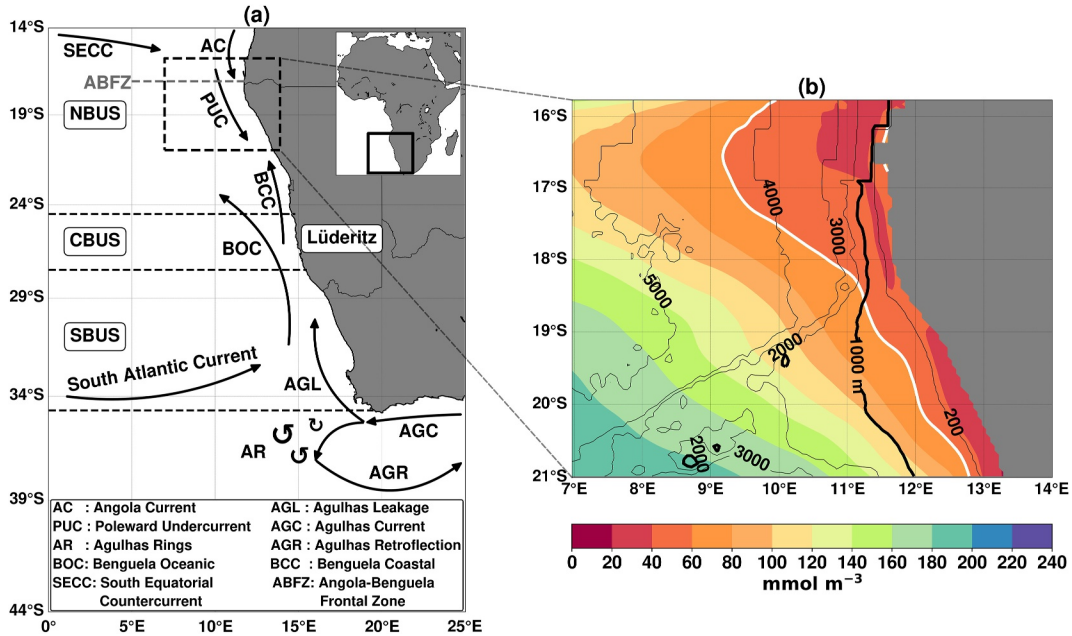

Figure 1. (a) Major oceanic circulation features of the Benguela Upwelling System (indicated by arrows) (Flohr et al., 2014; Verheye et al., 2016). Horizontal dashed lines delineate the three Benguela sub-regions: Northern (NBUS), Central (CBUS), and Southern (SBUS). The dashed box outlines the NBUS domain selected in this study. (b) Long-term climatology (1980–2020) of dissolved oxygen concentrations (mmol m^{-3}) at 100 m depth derived from Salama et al. (2025), where the white bold line indicates the limit of hypoxic waters (<60 mmol m^{-3}). Black contours represent the bathymetry derived from the GEBCO data set (GEBCO Compilation Group, 2021) as described in Salama et al. (2025), and the bold black line marks the 1,000 m depth level.

allowing cold, nutrient-rich deep waters to rise and fuel primary production (García-Reyes et al., 2015; Kämpf et al., 2016). The BUS exhibits pronounced spatial heterogeneity, with a division at the Lüderitz upwelling cell (~26°S), also referred to as the central BUS (CBUS), separating it into the northern (NBUS) and southern (SBUS) subregions (Hutchings et al., 2009) (Figure 1a). A strong latitudinal gradient in DO exists, with the NBUS being characterized by persistent low-oxygen (<120 mmol m^{-3}) and hypoxic (<60 mmol m^{-3}) waters (Figure 1b), while DO levels increase progressively southward (Lovecchio et al., 2022; Mohrholz et al., 2008; Monteiro & van der Plas, 2006). This makes the NBUS a distinct low-oxygen subregion within the BUS.

Circulation patterns in the NBUS are highly dynamic and play a central role in modulating DO variability. This variability is primarily associated with two contrasting water masses: South Atlantic Central Water (SACW) and Eastern South Atlantic Central Water (ESACW). SACW originates in the Brazil–Malvinas Confluence (Flohr et al., 2014; Gordon, 1981) and flows eastward via the South Equatorial Undercurrent and the South Equatorial Countercurrent (Brandt et al., 2024; Siegfried et al., 2019). It continues as the Angola Current (Kopte et al., 2017), and eventually feeds the Poleward Undercurrent in the NBUS (Figure 1a) (Kopte et al., 2017; Mohrholz et al., 2008). Along its pathway through the South Atlantic and the equatorial current system before reaching the Angola Current, SACW is exposed to large fluxes of sinking organic matter from the upper ocean. Its remineralization enriches nutrients and depletes oxygen, making SACW nutrient-rich but oxygen-poor (down to ~60 mmol m^{-3}; Emeis et al., 2018; Mohrholz et al., 2008).

ESACW is formed when Agulhas leakage water mixes in the Cape region with ambient South Atlantic waters before being transported northward by the Benguela Current, which branches at 26°S into oceanic and coastal currents, while the latter transports ESACW further northward (Siegfried et al., 2019; Stramma & Peterson, 1990; Tim et al., 2018) (Figure 1a). ESACW is cooler, more oxygenated (250–300 mmol m^{-3}), and nutrient-poor compared to SACW (Mohrholz et al., 2008; Poole & Tomczak, 1999). Changes in the relative fractions and DO content of these water masses directly impact oxygen levels in the NBUS.

In addition, Antarctic Intermediate Water (AAIW) contributes to the Benguela current water masses and, indirectly, influences the NBUS. AAIW forms within the Antarctic Circumpolar Current, characterized by low

salinity and temperature (Shannon & O'Toole, 1999; Talley, 1996). It reaches the Cape Basin from both South Atlantic and Indian Ocean pathways, and subsequently moves northward within the Benguela Current as an intermediate water mass (P. Richardson & Garzoli, 2003; Rimaud et al., 2012), with the mixed water exiting the basin and migrating northward at 700–1,100 m depth (Rimaud et al., 2012). It is an important carrier of Southern Ocean nutrients (McKay et al., 2016; Sarmiento et al., 2004). However, its circulation and identification in the Benguela system remain difficult to constrain due to weak intermediate-level mean flows relative to mesoscale variability and intense mixing in the Cape Basin. This also contributes to its poor representation in previous numerical models (Garzoli & Gordon, 1996; P. Richardson & Garzoli, 2003; Rimaud et al., 2012; Siddiqui et al., 2023).

The interplay of physical and biogeochemical processes plays a key role in shaping DO levels in the NBUS, especially during seasonal upwelling. Upwelling peaks in austral winter (July–August) and spring (September–November) (Veitch et al., 2009) and brings nutrient-rich deep water into the upper layers (Mohrholz et al., 2008), which stimulates high primary production over the shelf. Coastal biological DO production can reach 33 mmol m^{-3} per day in freshly upwelled plumes, while DO consumption is dominated by zooplankton respiration in the upper 100 m, exceeding 1 mmol m^{-3} per day (Schmidt & Eggert, 2016). Below the mixed layer (~35 m) (Lovecchio et al., 2022), nitrification consumes DO at rates up to 0.21 mmol m^{-3} per day between 100 and 200 m, and detritus mineralization (0.3 mmol m^{-3} per day) dominates at 200–600 m depths (Schmidt & Eggert, 2016). These biogeochemical processes, combined with SACW intrusion, shape the vertical oxygen structure: the upper layer remains well-oxygenated (>200 mmol m^{-3}), while an oxygen minimum zone (OMZ) forms between 100 and 400 m, with DO often falling below 60 mmol m^{-3} near the shelf break (~300 m) (Lovecchio et al., 2022, 2025; Schmidt & Eggert, 2016). Overall, DO variability in the NBUS reflects (a) external forcing through the volume and oxygen content of SACW/ESACW intrusions and (b) internal regulation by NBUS circulation and local ecosystem production and respiration.

If upwelling intensifies under climate warming (Bakun, 1990; Sydeman et al., 2014), the supply of oxygen-poor water to the upper layers will likely increase (Bakun et al., 2015), yet stronger wind stress could simultaneously enhance turbulent mixing, weaken stratification, and then promote ventilation of surface layers (De Szoeke & Richman, 1981; Rogerson et al., 2025; Weeks et al., 2024). However, recent work has shown low confidence in multi-decadal trends of wind-driven upwelling across the Benguela Upwelling System (Bordbar et al., 2023). These contrasting responses highlight the complex influence of upwelling intensification, along with ocean warming, on DO dynamics.

Changes in DO content in the NBUS may have detrimental ecological and biogeochemical consequences. Pelagic species in the region experience physiological stress at DO levels below 150 mmol m^{-3} (Hampton et al., 1999; Stramma et al., 2012), making them vulnerable even to moderate oxygen declines. During 1994–1995, a strong intrusion of oxygen-poor waters combined with a Benguela Niño event led to a collapse in pelagic fish biomass (Gammelsrød et al., 1998; Heymans et al., 2004). Expansions of the OMZ may also disrupt trophic interactions. Some copepod species utilize the OMZ as a refuge from predators that cannot tolerate low oxygen conditions. Thus, further OMZ expansion could decrease exposure to predation (Ekau et al., 2018). Benthic ecosystems are similarly impacted: macrobenthic diversity has been shown to decline significantly in water masses with DO between 5 and 45 mmol m^{-3} (Hashim et al., 2024). Additionally, DO loss near the seafloor can enhance denitrification and phosphate efflux, shifting the nitrogen-to-phosphorus ratio in upwelled waters (Lachkar et al., 2024; Nagel et al., 2013). Furthermore, sustained DO decline may intensify sulfur plumes (Ohde & Dadou, 2018) and enhance the production of potent greenhouse gases such as N_2O (Arévalo-Martínez et al., 2019) and CH_4 (Sabbaghzadeh et al., 2021). Given these ecological and biogeochemical consequences, understanding the variability and mechanisms governing DO in the NBUS is essential.

Due to the over-imposition of physical circulation and biogeochemical processes in shaping DO variability (Monteiro & van der Plas, 2006), a comprehensive, integrated approach is essential for understanding long-term changes in the NBUS. However, progress is constrained by the lack of long-term, high-resolution observational data. Most in situ records in the region are spatially sparse and temporally limited, with observational efforts spanning only short periods (e.g., Lovecchio et al., 2022; Mohrholz et al., 2008, 2014). Consequently, modeling has become a key tool for investigating DO dynamics. Previous efforts, such as the 15-year NBUS-focused model by Schmidt and Eggert (2016), provide valuable insights but have a limited temporal coverage. Global gridded data sets like GOBAI (Sharp et al., 2023) and those by Ito et al. (2017) span longer periods but have coarse spatial

resolution (typically 1°), limiting their ability to resolve mesoscale features critical for DO variability. Additionally, interpolation methods tend to underestimate deoxygenation trends, capturing only about two-thirds of their actual magnitude (Ito et al., 2024), while coarse-resolution Earth System Models struggle to simulate regional-scale oxygen dynamics.

To overcome these limitations, we use the data produced by the modeling system of Salama et al. (2025), which consists of a high-resolution (∼7 km) coupled physical-biogeochemical configuration for the whole BUS region and covers the period 1980–2020. This configuration resolves key mesoscale and shelf-scale processes and includes an intermediate-complexity biogeochemical module. The modeling system has been validated against both climatological data sets and in situ observations, demonstrating good skill in reproducing the circulation and biogeochemical characteristics of the BUS. It also captures the spatial and seasonal variability of DO, as shown in Figures S1 and S2 and Texts S1 and S2 of Supporting Information S1.

This study aims to investigate long-term DO variability in the NBUS and address the following questions:

1. How has the DO content in the NBUS changed over the past four decades (1980–2020)?
2. What are the causal factors of DO changes over time and across depth layers?
3. How have the OMZs evolved in terms of spatial extent and volume?
4. What does the DO budget reveal about the processes regulating oxygen variability in the NBUS?
5. How might DO changes affect the ecological and biogeochemical dynamics of the NBUS?

The next section presents the framework and the data produced by the coupled physical–biogeochemical model, along with the methods used to compute DO trends, identify causal links, characterize OMZ dynamics, and quantify the oxygen budget. The subsequent sections outline the results, discuss their implications, and conclude the study.

2. Methods

2.1. Coupled Physical–Biogeochemical Model Description

Outputs from the coupled physical-biogeochemical modeling system of Salama et al. (2025) are used. The modeling system is based on the "Nucleus for European Modeling of the Ocean" (NEMO v4.2.2; Madec & the NEMO System Team, 2023) coupled offline with the "Biogeochemical Flux Model" (BFM v5.3; Vichi et al., 2023). NEMO is a three-dimensional, finite-difference ocean model that solves the primitive Navier-Stokes equations under hydrostatic and Boussinesq assumptions. The BFM resolves chemical and biological interactions involving six key elements—carbon, nitrogen, phosphorus, silicon, iron, and oxygen—which constitute the foundations of living functional groups and non-living organic components. The modeling setup of Salama et al. (2025) employs a two-way nesting approach, with a high-resolution regional domain at ∼7 km for the broader BUS, embedded within a global ocean configuration at ∼25 km resolution. The Benguela regional domain extends from 15.71°S to 44.89°S and from 7.03°W to 27.28°E, with 75 vertical levels, spanning a range from a few meters at the surface to approximately 200 m in the deep ocean. The near-surface atmospheric forcing data were obtained from the ERA5 reanalysis data set (Hersbach et al., 2020). At the air–sea interface, prescribed biogeochemical fluxes account for wet and dry nitrogen deposition (Hegglin et al., 2016) and dust deposition (Lovato et al., 2022), with the latter being used to derive the surface inputs of iron, phosphate, and silicate. Initial conditions for DO were derived from the World Ocean Atlas 2018 (Garcia et al., 2019). A spin-up simulation was conducted for the physical and biogeochemical components by repeating the 1980 forcing conditions over 15 annual cycles (the spin-up simulation output is available in the Supplementary Data of Salama et al. (2026) at https://doi.org/10.5281/zenodo.21069384.

In the water column, DO is simulated as a reactive tracer governed by the following advection-diffusion-reaction equation:

$$\frac{\partial \mathrm{DO}}{\partial t} = -u \cdot \nabla \mathrm{DO} + \nabla_H \cdot (A_H \nabla_H \mathrm{DO}) + \frac{\partial}{\partial z}\left(A_V \frac{\partial \mathrm{DO}}{\partial z}\right) + \left.\frac{\partial \mathrm{DO}}{\partial t}\right|_{\mathrm{air-sea}} + \left.\frac{\partial \mathrm{DO}}{\partial t}\right|_{\mathrm{bio}}, \quad (1)$$

where $u \equiv (u, v, w)$ is the three-dimensional current velocity, A_H and A_V are the horizontal and vertical turbulent diffusivity coefficients for tracers. The $\frac{\partial \mathrm{DO}}{\partial t}\big|_{\mathrm{air-sea}}$ is the flux at the air-sea interface, and is modeled following the best practices reported in Orr et al. (2017) as:

$$\left.\frac{\partial \mathrm{DO}}{\partial t}\right|_{\mathrm{air-sea}} = K_w (DO_{\mathrm{a}} - DO_{\mathrm{w}}) \tag{1a}$$

where DO_{a} and DO_{w} are the concentrations in the atmospheric boundary layer and the seawater surface layer, respectively, and K_w is the gas transfer velocity, parameterized as a function of wind speed (see details in Wanninkhof, 2014). The term $\frac{\partial \mathrm{DO}}{\partial t}\big|_{\mathrm{bio}}$ represents biogeochemical transformation processes, which are formulated as:

$$\left.\frac{\partial\, \mathrm{DO}}{\partial t}\right|_{\mathrm{bio}} = \Omega_C^o \sum_{j=1}^{3} \left.\frac{\partial P_c^{(j)}}{\partial t}\right|_{\mathrm{DIC}}^{\mathrm{GPP}} - \Omega_C^o \left.\frac{\partial\, \mathrm{Comm}}{\partial t}\right|_{\mathrm{DIC}}^{\mathrm{RSP}} - \Omega_N^o \left.\frac{\partial\, \mathrm{NH_4^+}}{\partial t}\right|_{\mathrm{NO_3^-}}^{\mathrm{NIT}} - \Omega_C^o \left.\frac{\partial\, \mathrm{DIC}}{\partial t}\right|_{z=h}^{\mathrm{BEN}}, \tag{2}$$

where the upper indices denote the biogeochemical processes, while the lower indices indicate the tracer with respect to which the rate of change is formulated. GPP, RSP, NIT, and BEN denote gross primary production, respiration, nitrification rates, and consumption due to benthic remineralization, respectively. DIC is dissolved inorganic carbon; $\Omega_C^o = 0.083\ \left(\mathrm{mmol\ O_2\ mgC^{-1}}\right)$ is the carbon-to-oxygen conversion factor and $\Omega_N^o = 0.143\ \left(\mathrm{mmol\ O_2\ mgN^{-1}}\right)$ is the one for nitrogen-to-oxygen. $z = h$ denotes the seafloor depth. $\mathrm{NO_3^-}$ refers to nitrate and $\mathrm{NH_4^+}$ to ammonium concentrations, respectively. The community respiration (Comm) includes the respiration of phytoplankton (P_c), bacterial (B_c), and zooplankton (Z_c) functional groups according to the following equation:

$$\left.\frac{\partial\, \mathrm{Comm}}{\partial t}\right|_{\mathrm{DIC}}^{\mathrm{RSP}} = \sum_{j=1}^{3} \left.\frac{\partial P_c^{(j)}}{\partial t}\right|_{\mathrm{DIC}}^{\mathrm{RSP}} + f_B^o \left.\frac{\partial B_c}{\partial t}\right|_{\mathrm{DIC}}^{\mathrm{RSP}} + \sum_{j=4}^{6} \left.\frac{\partial Z_c^{(j)}}{\partial t}\right|_{\mathrm{DIC}}^{\mathrm{RSP}}. \tag{2a}$$

Here, f_B^o is a non-dimensional regulation factor representing the fraction of bacterial respiration occurring under aerobic conditions (see Vichi et al., 2023 for details). Gravitational sinking of particulate organic matter is resolved by means of a first-order scheme with a vertically uniform and constant sinking speed set to 1.0 m $\mathrm{d^{-1}}$.

The pelagic-benthic coupling in this configuration is represented through a simplified benthic closure that explicitly resolves the burial of particulate organic matter in the sediment and the fluxes of inorganic nutrients toward the bottom of the water column at prescribed remineralization rates (Lovato et al., 2022; Soetaert et al., 2000). Although oxygen is not dynamically resolved in the sediments, the same remineralization rates apply as well to sediment carbon content, in a respiration-like process, that determines the production of DIC and the consumption of DO in the above water cell.

The model data set used accounts for monthly averaged DO concentrations spanning the period from January 1980 to December 2020 (~4 decades). For the present study, we focus on the NBUS subregion spanning 7°E–14°E and 15.7°S–21°S (Figure 1a; dashed black box) and extending from the surface to 1,000 m depth (All analyses presented in this study are computed over this domain unless stated otherwise). DO concentrations are defined at the center of the three-dimensional grid cells, with the deepest center located at ~950 m. For depth- and volume-integrated DO, the full cell thickness is included, extending integration to the maximum depth of 1,000 m.

Here, we focus on the upper 1,000 m of the NBUS, where low-oxygen, hypoxic, and anoxic conditions are largely confined to the continental shelf and slope (Mohrholz et al., 2008; Monteiro & van der Plas, 2006; Schmidt & Eggert, 2016). This depth range also encompasses the OMZs (Meiritz et al., 2024), captures the influence of SACW and ESACW intrusions (Mohn et al., 2025), and includes upwelling-driven processes and associated biological activity (Siegfried et al., 2019).

2.2. Trends in Dissolved Oxygen Concentration

For trend analyses, de-seasonalized DO time series (monthly climatology removed) were used to compute long-term trends, considering only statistically significant results (p-value < 0.05), with oxygen inventory quantified by integrating concentrations over the entire NBUS volume. We derived oxygen saturation concentration (DO_{sat}) and Apparent Oxygen Utilization (AOU) to separate, respectively, the thermal and non-thermal components of oxygen variability. DO_{sat} represents the equilibrium oxygen solubility, and it was computed by the GSW Python package (IOC et al., 2010), using monthly conservative temperature and absolute salinity. AOU serves as a proxy for all processes other than saturation (see e.g., Busecke et al., 2022; Ditkovsky et al., 2023) and was computed as $\mathrm{AOU} = DO_{\mathrm{sat}} - \mathrm{DO}$.

2.3. SACW and ESACW Fractions

The fractions of the SACW and ESACW water masses were determined using temperature-salinity (T-S) characteristics. SACW was defined within an in situ temperature range of 8–16°C and a practical salinity range of 34.7201–35.6366, based on CTD and water samples collected in April 1999 from the central Angola Gyre (Mohrholz et al., 2008). ESACW was identified following the T–S properties reported by Poole and Tomczak (1999), namely with an in situ temperature interval of 5.9559–14.4067°C and a practical salinity range of 34.4069–35.3016.

For each grid cell, the expected practical salinity was computed using the corresponding T-S characteristic line and compared with the model value using a tolerance of ±0.05 in practical salinity. The choice of using slightly less stringent thresholds was made to mitigate the less-than-perfect reproduction of salinity, as biases were shown to affect simulated fields in the NBUS area (Salama et al., 2025). After identifying the grid cells satisfying the SACW or ESACW characteristics, the corresponding water volume was determined. Grid cells that did not satisfy either set of T–S criteria were not assigned to SACW or ESACW (i.e., the method does not impose a two-endmember partitioning of the full water column) and may therefore represent other water masses or mixed waters present in the NBUS.

The fraction (%) of each water mass was then calculated as the ratio between (a) the volume of classified grid cells summed horizontally and (b) the total water volume of the whole domain summed horizontally, yielding percentages as a function of time and depth. Finally, the analysis was restricted to the 100–1,000 m depth range, where these central waters are mostly prevalent (Mohn et al., 2025; Veleda et al., 2012). All calculation details are provided in Salama et al. (2026, https://doi.org/10.5281/zenodo.21069384).

2.4. Causal Discovery

To identify the key causal factors of DO variability in the NBUS, we employed the Peter and Clark Momentary Conditional Independence (PCMCI) algorithm (Runge et al., 2019). PCMCI is a causal discovery method for multivariate time series that determines statistically significant, time-lagged, and directional causal relationships between variables. Unlike correlation-based approaches, PCMCI isolates direct causal effects by accounting for indirect influences. This makes it well-suited for the complexity of the simulated DO (Section 2.1), where multiple interacting causal variables operate simultaneously. The PCMCI framework combines two steps: the Peter and Clark (PC) algorithm, which filters out spurious or indirect associations via conditional independence testing, and the Momentary Conditional Independence (MCI) test, which quantifies the strength and direction of retained causal links. Assuming a unit time lag, a variable X_{t-1} is considered (causal) for Y_t if changes in X at a preceding time $(t-1)$ contribute to changes in Y (target) at the current time step (t), after adjusting for other influencing variables. PCMCI relies on standard assumptions of causal inference, including the Markov condition, faithfulness, causal sufficiency, stationarity, and the exclusion of contemporaneous links. A thorough description of the method is given in Runge et al. (2019).

In this study, the algorithm is employed using the TIGRAMITE Python package (Runge et al., 2019, 2023), with partial correlation used to estimate causality effect sizes (i.e., MCI). Partial correlation values range from −1 to 1, indicating positive or negative causal relationships (i.e., positive or negative correlations between the causal variable and the target variable). Only links with $p < 0.05$ were retained. PCMCI was applied to monthly time series with a lag time window from 1 to 4 months, chosen to match the seasonal timing of processes influencing DO variability, such as upwelling dynamics and SACW/ESACW intrusions (Hagen et al., 2001; Schmidt &

Table 1
List of Variables Used in the PCMCI Causal Discovery Algorithm to Explain DO Time-Series Variability; the Table Includes Units and Definitions or Calculation Methods for Each Variable

Variable	Unit	Calculation/Definition
Physical Variables		
Oxygen Saturation (DO_{sat})	mmol m^{-3}	Defined as in Section 2.2
Apparent Oxygen Utilization (AOU)	mmol m^{-3}	Estimated as $AOU = DO_{sat} - DO$
Turbulent Kinetic Energy (TKE)	m^2 s^{-2}	Computed as $TKE = \frac{1}{2}(u'^2 + v'^2 + w'^2)$, where u', v' and w' are velocity anomalies from their long-term means (1980–2020)
Ocean Heat Content (OHC)	J m^{-2}	Computed as $OHC = \rho \cdot C_p \cdot T \cdot \Delta z$, where ρ is seawater density (kg m^{-3}) computed using the GSW package (IOC et al., 2010); C_p is the specific heat capacity of seawater (~3991.87 J kg^{-1} K^{-1}); T is conservative temperature in Kelvin; and Δz is the vertical thickness of the grid cell (m)
Brunt–Väisälä Frequency (BVF)	s^{-2}	Defined as $N^2 = -\frac{g}{\rho}\frac{\partial \rho}{\partial z}$, where g is the gravitational acceleration, ρ is the potential density, and $\frac{\partial \rho}{\partial z}$ is the vertical density gradient
Mixed Layer Depth (MLD)	m	Defined in NEMO as the turbocline depth
Meridional Wind Stress (τ_y)	N m^{-2}	Computed as $\tau_y = \rho_a C_d \lvert \mathbf{U} \rvert V$, where ρ_a is air density (1.22 Kg m^{-3}), C_d is the drag coefficient (1.3×10^{-3}), $\lvert \mathbf{U} \rvert$ is the wind speed magnitude, and V is the meridional wind velocity at 10 m derived from ERA5 re-analysis data (Hersbach et al., 2020). The calculation is restricted to alongshore winds with $V > 5$ m s^{-1}, since upwelling tends to only occur when wind exceeds that speed (Abrahams et al., 2021)
SACW and ESACW Fractions	%	Computed as reported in Section 2.3
Biogeochemical Variables		
Gross Primary Production (GPP)	mmol m^{-3} d^{-1}	Total phytoplankton production
Net Primary Production (NPP)	mmol m^{-3} d^{-1}	GPP—Total phytoplankton respiration
Community Respiration (Comm)	mmol m^{-3} d^{-1}	Total respiration of living functional groups (see Equation 2a)

Eggert, 2016; Veitch et al., 2009). All variables' time series were de-seasonalized to isolate sub-seasonal to interannual variability. The multivariate data set included the most relevant physical and biogeochemical variables affecting DO variability in an upwelling system like the NBUS (see Table 1). Variables were selected based on their mechanistic roles in oxygen dynamics, including: alongshore wind stress (τ_y), upper-ocean mixing (TKE, turbulent kinetic energy; MLD, mixed layer depth), the influence of ocean heat content (OHC) and stratification (BVF, Brunt–Väisälä frequency), the intrusion of oxygen-poor or oxygen-rich water masses (SACW and ESACW), as well as biological processes that add oxygen through primary production (NPP) or consume it through community respiration (Comm). As our analysis considered a rather large number of variables, we here adopted a tabular representation of the PCMCI outcomes rather than the classic causal graph (see e.g., Runge et al., 2019). In this matrix, the causal direction reads from the variables reported on rows (causal variables) to those on columns (target variables), where grid-cell colors show MCI values, numbers indicate time lags, and empty cells indicate no causal link. When multiple significant links exist between a causal–target pair at different time lags, only the link with the strongest absolute MCI value is retained. The relation of a causal variable with its own past state, referred to as Auto-MCI, is reported along the diagonal of the matrix. In the PCMCI, Auto-MCI quantifies the time-lagged self-dependence of a variable, that is, whether its past state (X_{t-1}) exerts a statistically significant causal influence on its present state (X_t) after conditioning on all other variables. Empty diagonal Auto-MCI entries indicate that no significant lagged self-dependency was detected, implying that the variable does not exhibit statistically significant causal dependence on its own past state within the tested lag window.

2.5. Oxygen Minimum Zones Definition

OMZs are defined as areas where oxygen concentrations fall below specific thresholds. In this study, OMZ boundaries were analyzed across three key thresholds: the OMZ core with water masses having $DO < 20$ mmol m^{-3} (OMZ_{20}), hypoxic waters with $DO < 60$ mmol m^{-3} (OMZ_{60}), and low-oxygen waters where $DO < 120$ mmol m^{-3} (OMZ_{120}). The upper and lower boundaries of each OMZ threshold were determined for

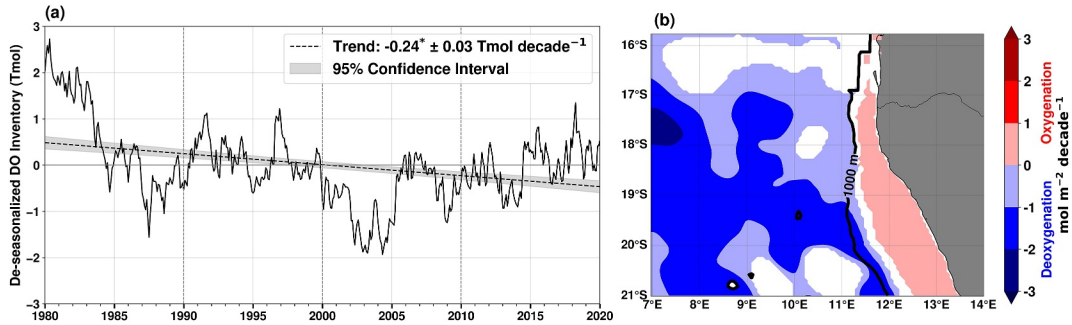

Figure 2. (a) Time series of monthly dissolved oxygen (DO) inventory, de-seasonalized by removing the 1980–2020 monthly climatology, and spatially integrated over the selected NBUS domain (0–1,000 m). Gray shading indicates the 95% confidence interval, while the black dashed line represents the linear trend. The trend value is indicated along with the standard error. (b) Long-term trend of vertically integrated (0–1,000 m) de-seasonalized DO inventory for the period 1980–2020. Positive values indicate oxygenation and negative ones deoxygenation. Grid cells with non-significant trends (p-value > 0.05) are excluded (white areas). The bold black line marks the 1,000 m seabed depth.

each horizontal grid cell by identifying the depths where oxygen concentrations match the corresponding threshold. At each location, the vertical thickness of each OMZ was calculated as the difference between its lower and upper boundaries. OMZ volume was calculated by summing the volume of all grid cells where oxygen concentrations fall below the specified threshold, such that OMZ_{60} fully contains OMZ_{20}, and OMZ_{120} encompasses both OMZ_{20} and OMZ_{60}. Here, we do not consider the full water column OMZ volume but rather only the 0–1,000 m layer, consistent with the vertical extent of the investigated NBUS domain (see Section 2.1).

2.6. DO Budget Calculation

The DO budget was computed by quantifying both physical and biogeochemical oxygen fluxes within the NBUS domain (Figure 1a; dashed black box). Physical oxygen fluxes were calculated across the top, bottom, and lateral boundaries of the NBUS domain. At the lateral and bottom boundaries, fluxes were obtained by multiplying DO concentrations (mmol m^{-3}) (without de-seasonalization) by the respective water volume transport rates (m^3 s^{-1}), yielding DO fluxes in mmol s^{-1}. These fluxes were computed for each grid cell along each boundary of the NBUS domain (top, bottom, and lateral boundaries) and subsequently summed over all grid cells belonging to that boundary. At the top boundary, air–sea DO exchanges (mmol m^{-2} s^{-1}) were obtained directly from the biogeochemical model outputs (see Section 2.1) and integrated over the surface area (m^2) of the NBUS domain to obtain total oxygen fluxes in mmol s^{-1}. The inner-ocean biogeochemical contributions were quantified by integrating GPP and community respiration rates over the NBUS domain volume.

All fluxes were computed as per-second rates and integrated over the simulation period (1980–2020), using the total number of seconds in 41 years, to obtain cumulative values over the full simulation period. Positive and negative flux values were separated, where positive flux values indicate oxygen entering the NBUS domain through lateral, top, and bottom boundaries or produced via GPP, while negative values represent oxygen losses through boundary outflows and biological consumption due to respiration.

3. Results

3.1. Trends in DO Inventory in the NBUS

The de-seasonalized time series of total DO inventory (Figure 2a) shows a statistically significant negative trend of −0.24 ± 0.03 Tmol per decade, indicating a total decline in DO over the 1980–2020 period. Despite this long-term decline, the de-seasonalized inventory exhibits considerable decadal-scale variability. A marked decrease occurs in the first decade (1980–1990), with values falling from 2 to −0.5 Tmol. The second and third decades show pronounced fluctuations rather than a consistent decline. In contrast, the last decade (2011–2020) displays an increase, with values rising from −0.2 to 0.5 Tmol. While the recent decade suggests a partial recovery, the overall trend still reflects significant deoxygenation over the full period.

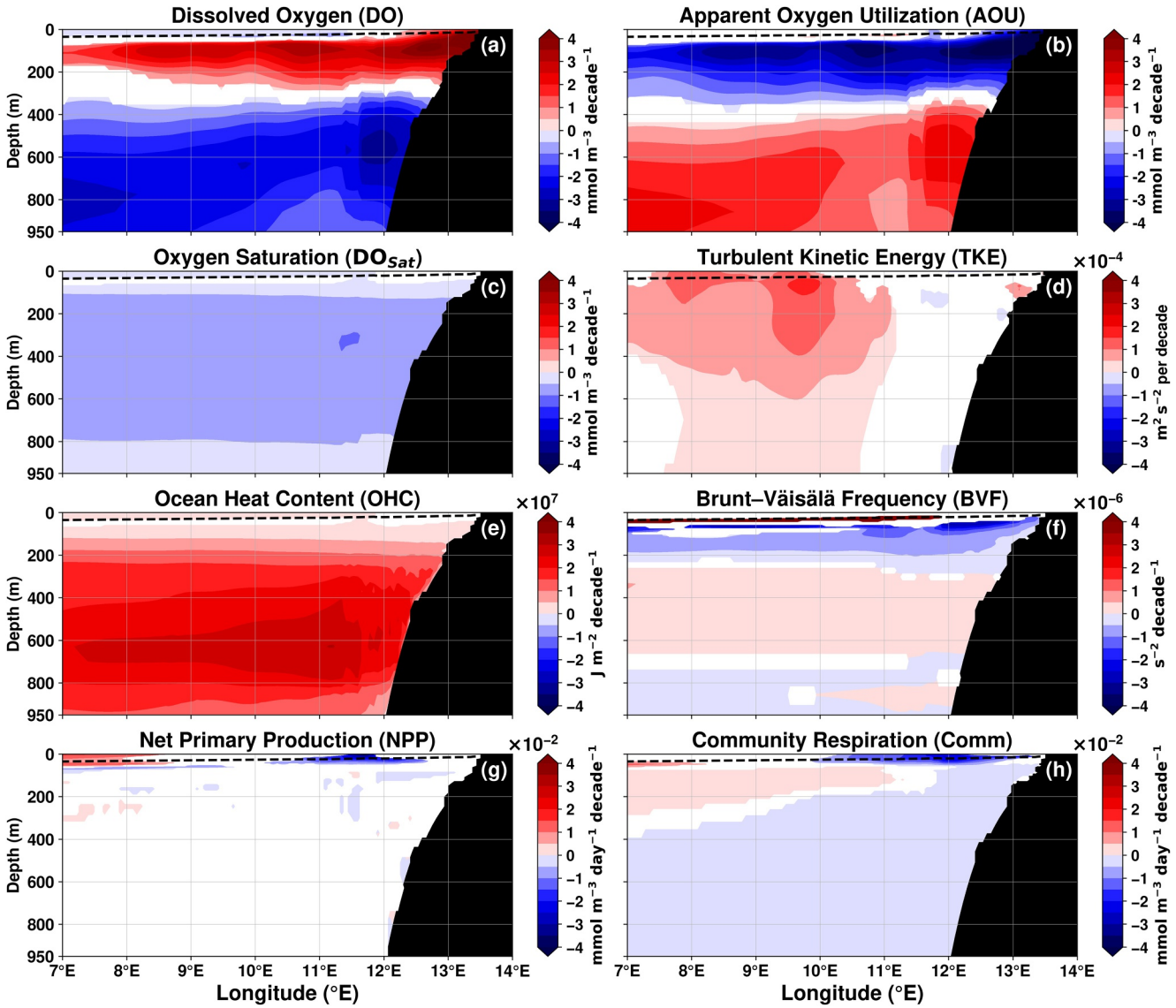

Figure 3. Linear trends over the period 1980–2020 for latitudinally averaged, de-seasonalized fields over the NBUS domain (shown in Figure 1a; dashed black box): dissolved oxygen concentrations (a), AOU (b), DO_{sat} (c), TKE (d), OHC (e), BVF (f), NPP (g), and Community Respiration (h). White areas indicate regions where the trends are not statistically significant ($p > 0.05$). All trends are expressed as changes per decade. Black dashed lines represent the long-term climatology of MLD, and the continental shelf is shown in black.

The long-term trend of vertically integrated (0–1,000 m) DO inventory reveals a clear contrast between shelf and offshore regions (Figure 2b). Along the shelf, a statistically significant oxygenation tendency is evident, reaching up to 0.7 mol m^{-2} per decade and extending offshore about 150 km from the coastline. In contrast, the open ocean exhibits a significant deoxygenation trend, with values reaching −2.4 mol m^{-2} per decade. These contrasting trends highlight the spatial complexity of oxygen dynamics in the NBUS.

3.2. Vertical Structure of DO Trends and Associated Causal Variables

Linear trend analysis was conducted on the latitudinally averaged DO concentrations, together with physical and biogeochemical variables introduced in Section 2.4 and Table 1. The resulting trend patterns are shown in Figure 3.

DO trend results reveal a clear vertical dipole structure (Figure 3a): an oxygenation trend with values up to 5.4 mmol m^{-3} per decade in the upper 400 m, being more intense over the shelf region, and a deoxygenation trend

reaching −3.1 mmol m^{-3} per decade between 400 and 950 m. A weak deoxygenation trend is also evident in the upper ∼50 m of the open ocean region (7°E to 11.5°E), with values not exceeding −1 mmol m^{-3} per decade. The transition zone between the upper oxygenated and lower deoxygenated layers shows no statistically significant trend.

The analysis of thermal and non-thermal DO components indicates that DO trends are primarily influenced by non-thermal processes, as reflected in AOU trends (Figure 3b), with minimal contribution from DO_{sat} (see Figure S3 in Supporting Information S1). AOU trends closely match DO trends in magnitude but with opposite signs, highlighting that changes in processes other than saturation (e.g., circulation, mixing, biological activity, and/or other factors) are the main contributors to the revealed DO trends. AOU trends range from −5.5 to 2.4 mmol m^{-3} per decade, reinforcing their dominant role in shaping the dipole structure. In contrast, DO_{sat} trends are exclusively negative across the domain (Figure 3c), with values reaching up to −1 mmol m^{-3} per decade. However, the contribution of DO_{sat} to the DO trend is more pronounced in the upper 50 m of the open ocean region (7°E to 11.5°E) (Figure S3 in Supporting Information S1).

Trends in physical metrics, namely TKE, OHC, and BVF (Figures 3d–3f), show patterns that may help explain the contrasting DO trends. TKE trend is characterized by predominantly positive trends in the open waters, reaching up to 2×10^{-4} m^2 s^{-2} per decade (Figure 3d), equivalent to a 25% increase relative to the long-term climatology. These increases are most pronounced in the upper 400 m and offshore, with localized positive values over the shelf, highlighting enhanced turbulence in the upper layers. OHC also exhibits consistent positive trends across the domain, with a mean of $\sim 0.73 \times 10^7$ J m^{-2} per decade (Figure 3e), indicating pervasive warming, especially in deeper layers. In contrast, BVF trend displays a more structured pattern across depths (Figure 3f): negative trends dominate the upper 250 m, indicating weakening stratification, while positive trends between 250 and 650 m reach up to 1×10^{-6} s^{-2} per decade (∼4% increase relative to the climatological mean). Collectively, these trends suggest enhanced turbulence and reduced stratification in upper layers, along with increased stratification and warming at intermediate depths.

NPP and community respiration trends (Figures 3g and 3h) reveal rather contrasting patterns. NPP shows no statistically significant trends across most of the domain, with only a few positive and negative grid cells confined to the upper 50 m (Figure 3g). The community respiration exhibits predominantly negative trends throughout the water column, especially over the shelf, with values reaching up to −0.1 mmol m^{-3} day^{-1} per decade (Figure 3h), corresponding to a ∼4% decrease relative to the long-term mean. This suggests a long-term decline in oxygen consumption via respiration. Notably, positive community respiration trends appear between 50 and 200 m, particularly offshore, with maxima of 0.01 mmol m^{-3} day^{-1} per decade.

To further interpret the vertical structure in DO trends, we examined changes in MLD and τ_y to illustrate wind forcing in upper-ocean mixing. Trends in SACW and ESACW fractions are also introduced to assess how shifts in water mass composition may influence DO. We also explore why deoxygenation remains confined to deeper layers despite widespread warming.

The spatially averaged time series of MLD and τ_y over the NBUS domain (Figure 4a) exhibit statistically significant positive trends of 0.25 m per decade and 1.56×10^{-3} N m^{-2} per decade, respectively. Both variables are strongly correlated ($r = 0.71^*$), indicating that intensified τ_y is associated with a deepening of the mixed layer. Although the magnitude of the MLD trend suggests only a modest deepening, its coherence with the strengthening wind stress points to enhanced wind-induced turbulent mixing in the upper ocean. This finding is consistent with the positive trends previously identified in TKE (Figure 3d), reflecting wind-induced upper-ocean turbulence that may promote ventilation.

Regarding the SACW and ESACW fractions, their temporal and vertical variability is first presented in Figure S4 in Supporting Information S1. SACW dominates the NBUS study domain, with a long-term (1980–2020) mean fraction of about 58%, whereas ESACW exhibits a much lower mean contribution of approximately 9%. Both water masses extend vertically from 100 m down to nearly 500 m. Figure S4 in Supporting Information S1 further shows that the SACW fraction decreases markedly over time, with the strongest reduction occurring during the last decade (2010–2020), while ESACW displays comparatively weaker temporal variations. The long-term trends shown in Figure 4b quantify the linear change in the water-mass fraction, expressed in percentage per decade, over the 1980–2020 period. Both fractions exhibit a consistent negative trend; SACW shows the strongest decline, reaching up to −11% per decade within the 100–400 m range, coinciding with the simulated oxygenation

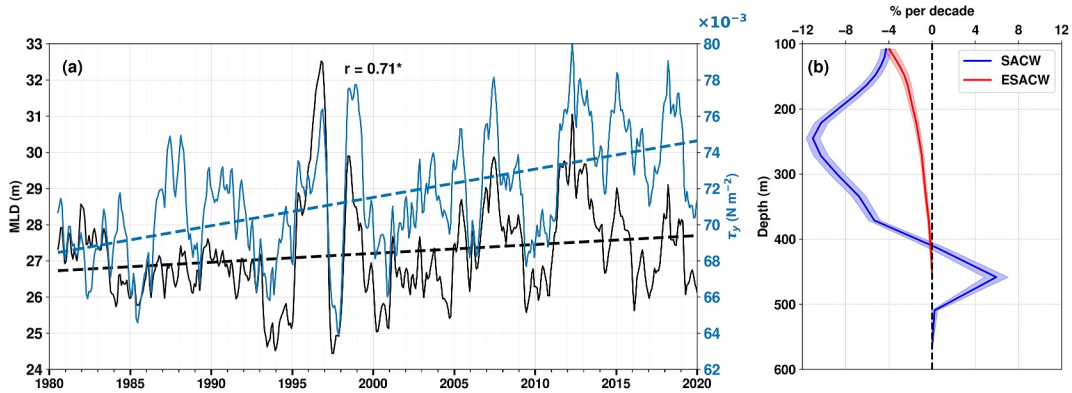

Figure 4. (a) NBUS domain-averaged time series of mixed layer depth (MLD; black) and meridional wind stress (τ_y; blue) from 1980 to 2020, de-seasonalized and smoothed using a 12-month moving average. Dashed lines represent the respective linear trends, and *r* indicates the correlation coefficient between both variables. (b) Vertical linear trends (1980–2020) of de-seasonalized South Atlantic Central Water (SACW; blue) and Eastern South Atlantic Central Water (ESACW; red) fractions, expressed as the linear change in the water-mass fraction (% per decade). Negative (positive) values indicate a reduction (increase) in the fractional contribution of waters satisfying the respective T–S definition in the NBUS domain. Shaded areas denote the 95% confidence intervals.

trend in the upper layers. This decrease indicates a reduction of SACW water masses entering the NBUS over time. In contrast, ESACW exhibits a smaller decrease, with maximum values of about −4% per decade, primarily confined to the upper 200 m.

Given that OHC exhibits a positive trend across the entire domain (Figure 3e), while deoxygenation remains confined to deeper layers, we examined the relationship between OHC and DO inventory across four depth intervals: 0–200 m, 200–400 m, 400–600 m, and 600–1,000 m (Figure 5). The correlation between vertically integrated, de-seasonalized OHC and DO (Figures 5a–5d) strengthens with depth, ranging from no significant correlation in the upper 200 m to strong negative correlations at 400–600 m and 600–1,000 m ($r = -0.79^*$ and $r = -0.93^*$, respectively). These patterns are consistent with the temporal trends shown in Figures 5a–5d, where the strongest deoxygenation occurs below 400 m, reaching −0.24 Tmol decade^{-1} at 600–1,000 m, accompanied by pronounced warming (0.3×10^{20} J decade^{-1}). Overall, although OHC increases throughout the water column, its deoxygenation influence is more pronounced in deeper layers.

Given its strong association with deep deoxygenation, we evaluated the simulated OHC variability against observational estimates derived from the ARMOR3D global ocean analysis (CMEMS, 2022) over the period 1993–2020. ARMOR3D provides gridded temperature and salinity fields at a spatial resolution of 25 km and combines in situ measurements with satellite observations using multiple linear regression methods that relate surface and subsurface data (Guinehut et al., 2012).

Figure S5 in Supporting Information S1 shows the comparison between simulated OHC and ARMOR3D estimates across four depth intervals. Overall, the model reproduces both the temporal variability and long-term evolution of OHC reasonably well. Both the model and observations exhibit statistically significant positive trends between 200 and 1,000 m over the 1993–2020 period. The correlation between simulated and observed OHC is statistically significant, with values ranging from 0.3 to 0.6. Both data sets further indicate that the strongest warming occurs in the 600–1,000 m layer. The model simulates a trend of 0.17×10^{20} J decade^{-1}, which is comparable to the ARMOR3D trend of 0.14×10^{20} J decade^{-1}. Overall, the agreement between simulated and observational OHC provides evidence that the model realistically captures the long-term vertical variability of OHC in the NBUS domain.

3.3. Causal Discovery of DO Variability

Following the vertical dipole structure of DO trends identified in Section 3.2, the PCMCI algorithm (see Section 2.4 for details about the algorithm) was applied separately to the upper (0–400 m) and deeper (400–1,000 m) layers. This separation allows the isolation of the distinct causal variables responsible for the contrasting vertical trends in DO. The analysis was based on the multivariate data set described in Table 1, including relevant physical

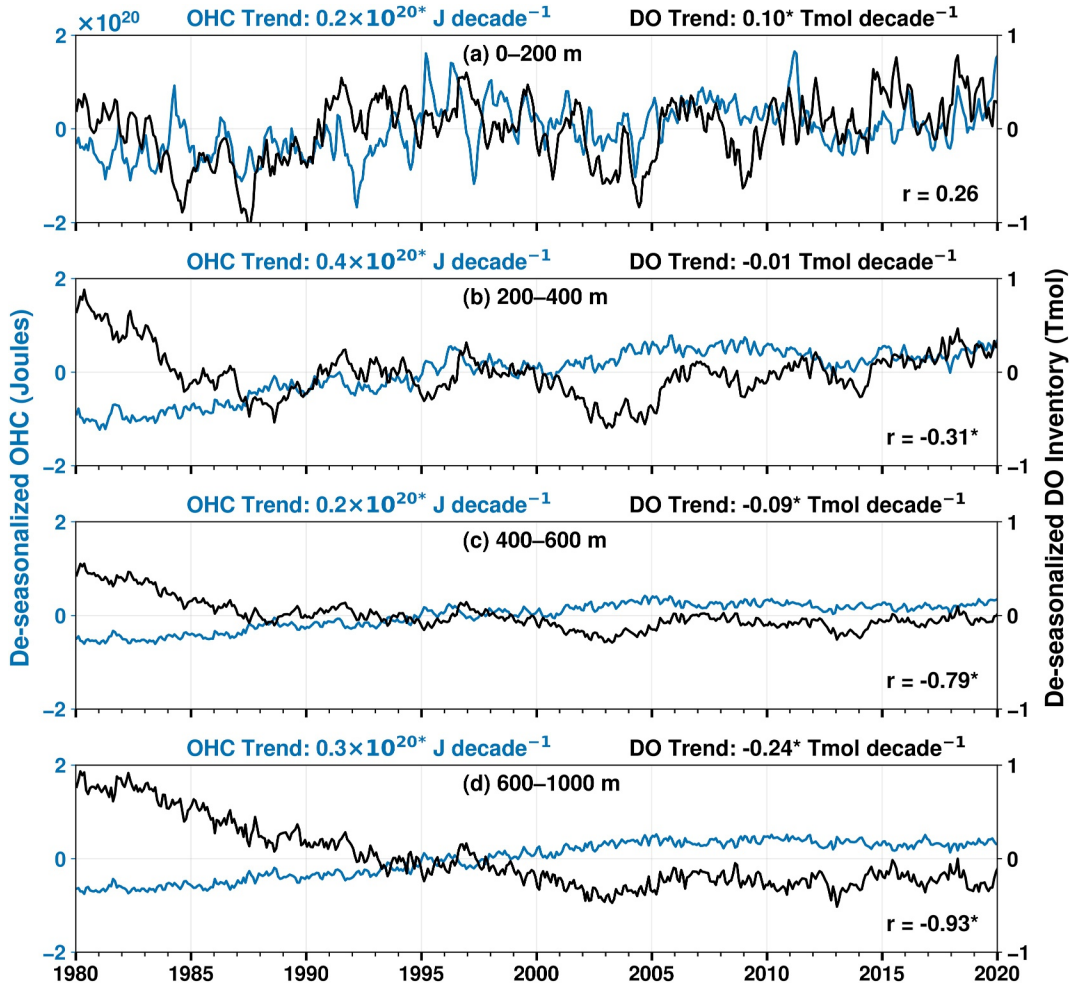

Figure 5. Temporal relationship between ocean heat content (OHC) and dissolved oxygen (DO) inventory in the NBUS domain across four depth intervals: 0–200 m, 200–400 m, 400–600 m, and 600–1,000 m. Panels (a–d) show de-seasonalized, spatially integrated time series of OHC (blue lines) and DO inventory (black lines), each vertically integrated over the corresponding depth interval. OHC trends (J decade^{-1}) and DO trends (Tmol decade^{-1}) are indicated above each panel. Pearson correlation coefficients between OHC and DO are shown in the lower right of each panel. Asterisks indicate statistical significance at $p < 0.05$.

and biogeochemical variables for each layer. To maintain causal consistency, variables known to have limited or negligible influence below 400 m, namely MLD, τ_y, NPP, SACW, and ESACW, were excluded from the deeper-layer analysis.

In the upper 0–400 m layer (Figure 6), DO variability is primarily controlled by physical processes associated with mixing and wind forcing. The strongest causal variables are MLD, TKE, and τ_y, with predominantly short lags (lag = 1 month) and MCI values of 0.26, 0.15, and 0.12, respectively, indicating a rapid response of near-surface oxygen to changes in vertical mixing and wind-driven circulation. Water-mass variability also contributes: SACW and ESACW exert causal influences of (MCI = −0.11 and +0.12, respectively), consistent with their contrasting oxygen characteristics. DO exhibits a strong Auto-MCI of +0.72 at lag = 1, indicating a strong dependence on its previous state. In the PCMCI framework, this high Auto-MCI reflects a statistically significant causal link between DO at time $t - 1$ and DO at time t, after conditioning on all other variables included in the analysis.

Regarding the thermal and non-thermal components of DO, AOU exhibits significant causal links with MLD and TKE (MCI = −0.43 and −0.24), highlighting the role of ventilation in reducing apparent oxygen utilization. In contrast, DO_{sat} has stronger causal links with τ_y and OHC, reflecting the combined effects of wind-induced

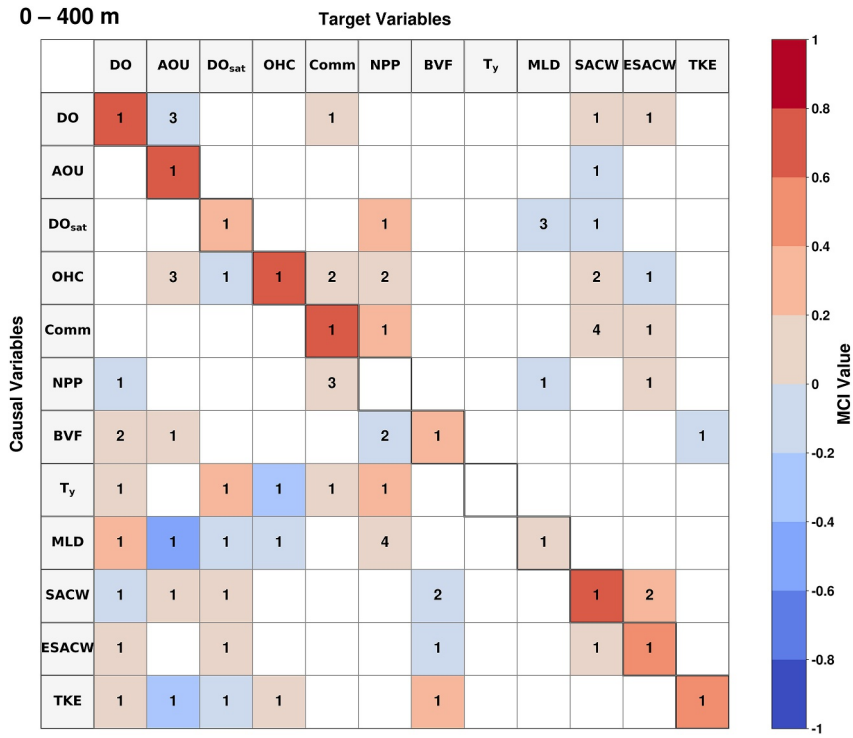

Figure 6. Causal discovery relationships of DO and associated variables (see Table 1 and Section 2.4) in the upper 400 m of the NBUS domain over the period 1980–2020. The time series used are monthly averaged and de-seasonalized. The variables on the rows of the matrix represent the causal variables, while those in the columns denote the corresponding target variables. Grid-cell colors indicate the MCI values, and the numbers represent the time lag (months). Diagonal cells report the auto-dependencies (Auto-MCI). When multiple significant links exist between a given causal–target pair at different time lags, only the link with the strongest absolute MCI value is retained (e.g., if significant links occur at lag 1 and lag 3, the one with the larger absolute MCI is shown). Empty white cells indicate that no statistically significant causal relationship was detected between the respective causal–target pair. Empty diagonal cells indicate the absence of statistically significant lagged self-dependence (Auto-MCI), meaning that the variable does not exhibit significant dependence on its own past state.

processes and temperature-dependent solubility. As τ_y can lead to changes in the upper-ocean heat balance, and consequently seawater temperature, it can therefore affect DO_{sat}.

In the 400–1,000 m layer (Figure 7), the causal structure shifts toward subsurface controls. The strongest negative influence on DO arises from BVF (MCI = −0.19 at lag = 2), followed by OHC (MCI = −0.18 at lag = 1). These links indicate that enhanced stratification and warming suppress vertical oxygen replenishment, thereby contributing to deoxygenation at depth. Moreover, OHC exerts a strong negative influence on DO_{sat} (MCI = −0.69 at lag = 1), reinforcing the dominant role of subsurface warming in controlling oxygen saturation. The Auto-MCI of DO (= −0.14 at lag = 2) in the 400–1,000 m layer is comparatively weak, indicating that past DO values have only a limited causal influence on its present state.

Overall, the layer-separated PCMCI analysis provides a mechanistic explanation for the vertical dipole: upper-layer DO variability is governed mainly by wind-driven mixing processes acting at short time-lags, whereas deeper-layer DO variability is primarily controlled by stratification and warming, reflecting reduced vertical oxygen replenishment.

The complete PCMCI results, together with their corresponding *p*-values and rankings, are provided in Text S3 and Tables S1 and S2 in Supporting Information S1.

3.4. OMZ Thresholds in the NBUS: Spatial Variability and Long-Term Trends

Climatological means of OMZ boundaries, thickness, volumes, and associated trends are provided in Table 2. The long-term climatology (1980–2020) of OMZs in the NBUS reveals clear spatial contrasts among the OMZ_{20},

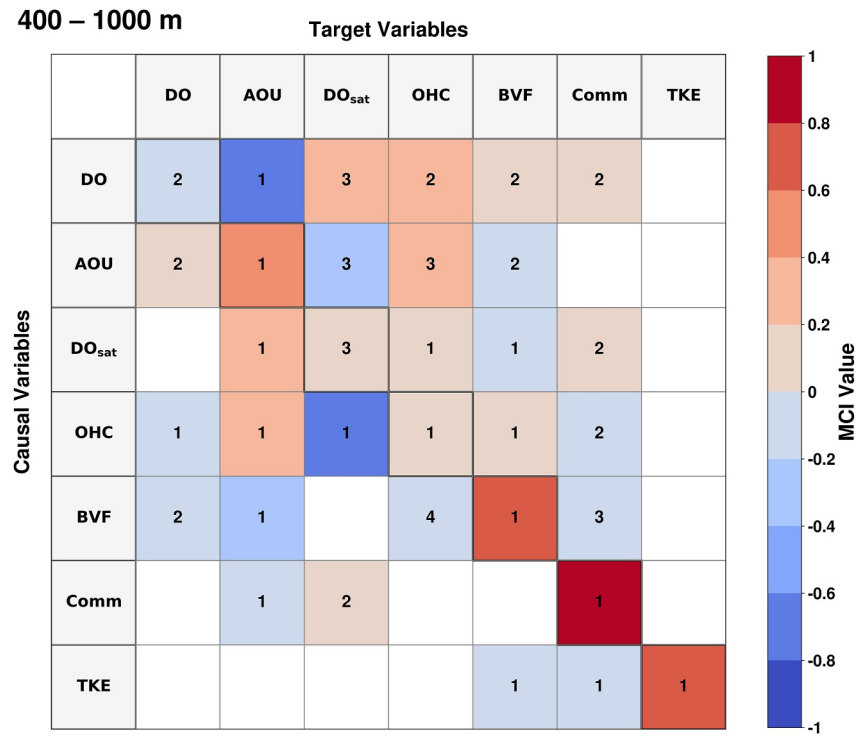

Figure 7. Causal discovery relationships of DO and associated variables (see Table 1 and Section 2.4) in the 400–1,000 m depth range of the NBUS domain evaluated over the period 1980–2020. Details about the matrix are similar to those shown in Figure 6.

OMZ_{60}, and OMZ_{120} thresholds (Figure 8). OMZ_{20} (Figures 8a–8c) is the most spatially restricted, both vertically and horizontally. Both the upper (Figure 8a) and lower (Figure 8b) boundaries of the OMZ_{20} are primarily confined to nearshore waters within a depth range of 100–200 m. This results in a relatively thin vertical layer, with a maximum of ∼100 m (Figure 8c).

The hypoxic OMZ_{60} (Figures 8d–8f) displays a broader vertical and lateral extent. The upper boundary lies within the upper 100 m nearshore and deepens to around 200 m offshore. The lower boundary spans from 200 to 300 m

Table 2
Long-Term Characteristics of OMZs (Upper and Lower Boundaries, Vertical Thickness) and Total Integrated Volume in the NBUS Over the Period 1980–2020; for Boundaries and Thickness, Mean Values (± Standard Deviation) Are Calculated Across the Domain, While Trends Represent the Average Change per Decade Across Grid Cells; for Total Volume, Values Correspond to the Domain-Integrated Volume; Asterisks Denote Statistically Significant Trends at p-Value < 0.05

OMZ	Upper boundary (m)	Lower boundary (m)	Vertical thickness (m)	Total volume (km^3)
OMZ_{20}				
Mean ± STD	127 ± 21	166 ± 33	40 ± 17	682
Trend per decade	3*	−10*	−6*	−436*
OMZ_{60}				
Mean ± STD	129 ± 34	346 ± 127	218 ± 131	55,625
Trend per decade	4*	11*	7*	454
OMZ_{120}				
Mean ± STD	114 ± 65	701 ± 225	586 ± 223	198,251
Trend per decade	3*	15*	13*	4,154*

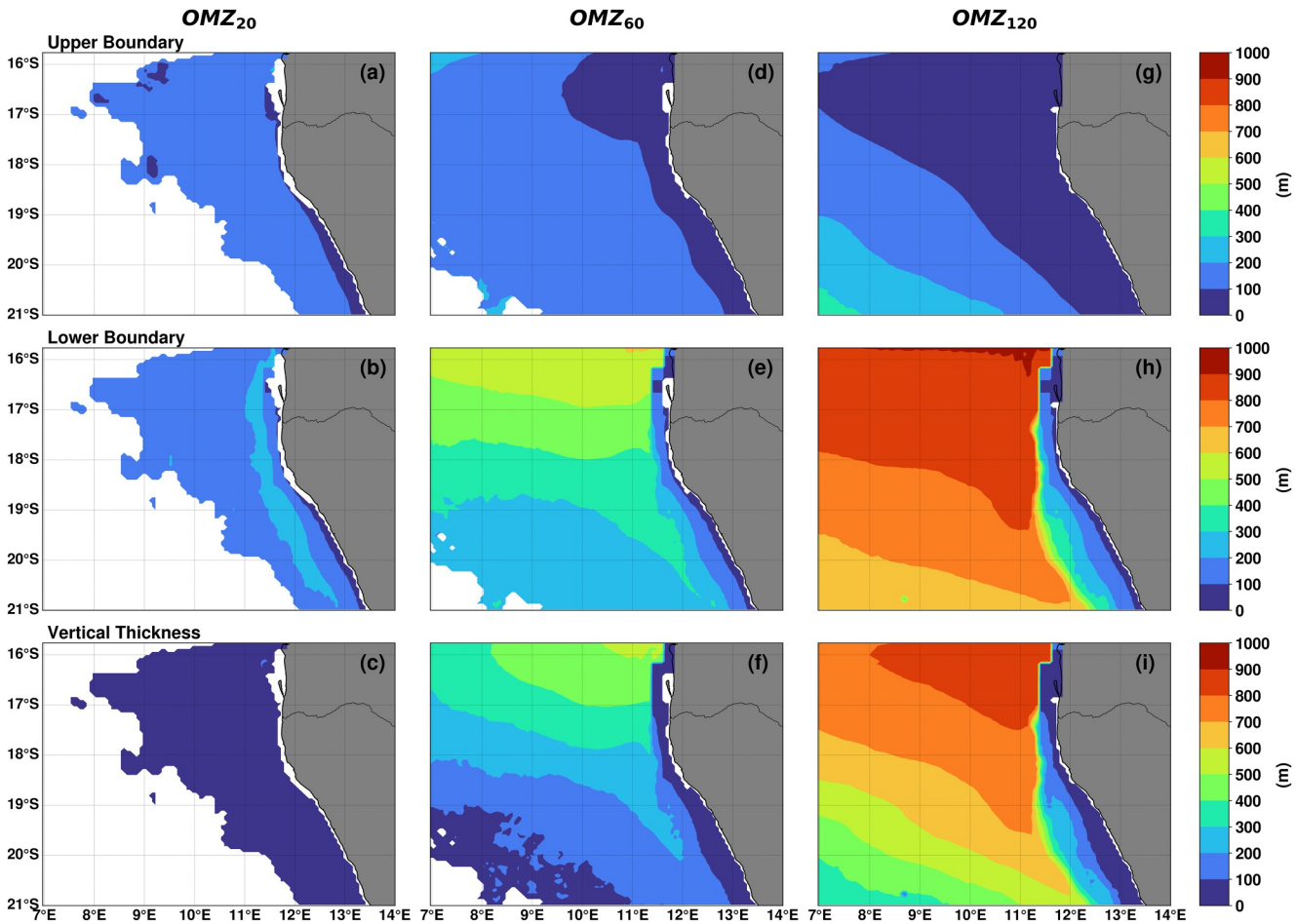

Figure 8. Long-term annual climatology (1980–2020) of Oxygen Minimum Zone (OMZ) thresholds in the Northern Benguela Upwelling System. Columns correspond to the selected OMZ thresholds (see Section 2.5) of 20, 60, and 120 mmol m^{-3}, respectively. Rows represent the upper boundary depth, lower boundary depth, and vertical thickness in meters for each OMZ threshold, respectively. Accordingly, panels (a, d, g) show the upper boundary depth, panels (b, e, h) show the lower boundary depth, and panels (c, f, i) show the vertical thickness for OMZ_{20}, OMZ_{60}, and OMZ_{120}, respectively.

between 18.5°S and 21°S and reaches depths of up to 600 m in the northern areas (15.7°S–17°S), resulting in a markedly thicker OMZ layer in offshore regions.

The OMZ_{120} (Figures 8g–8i) is the most spatially extended of the three thresholds, dominating the NBUS domain. Its upper boundary (Figure 8g) is shallow near the coastal upwelling zone (from the surface down to ~100 m) and gradually deepens offshore to 100–330 m between 7°E–10°E and 19°S–21°S. The lower boundary (Figure 8h) closely follows the continental slope, descending from ~400 m near the shelf break to ~900 m in the open ocean. In the northern region, OMZ_{120} reaches its maximum vertical thickness, often exceeding 800 m (Figure 8i).

The long-term trends of the OMZs thresholds (Figure 9) show that the vertical boundaries of OMZ_{20} exhibit statistically significant trends only at a few locations (Figures 9a–9c). Within these limited areas, particularly in the far northern part of the domain (15.7°S–16.3°S), the lower boundary shows a shoaling trend with values reaching up to ~20 m per decade (Figure 9b), leading to localized thinning of the OMZ_{20} layer (Figure 9c). This pattern is reflected in a statistically significant decline in OMZ_{20} volume, with a trend of −436 km^3 per decade (Figure 9d). This trend is associated with a sharp compression of the OMZ_{20}, with its volume declining from a mean of 1,708 km^3 in the first decade (1980–1990) to a mean of 73 km^3 in the last decade (2010–2020).

OMZ_{60} (Figures 9e–9g) displays a weak deepening trend in the upper boundary, especially in nearshore and northern regions, with values reaching up to 17 m per decade (Figure 9e). The lower boundary exhibits a more pronounced deepening, particularly beyond the shelf break, with trends up to 25 m per decade (Figure 9f). These changes result in widespread thickening of the OMZ_{60} layer, with maximum trends of 25 m per decade

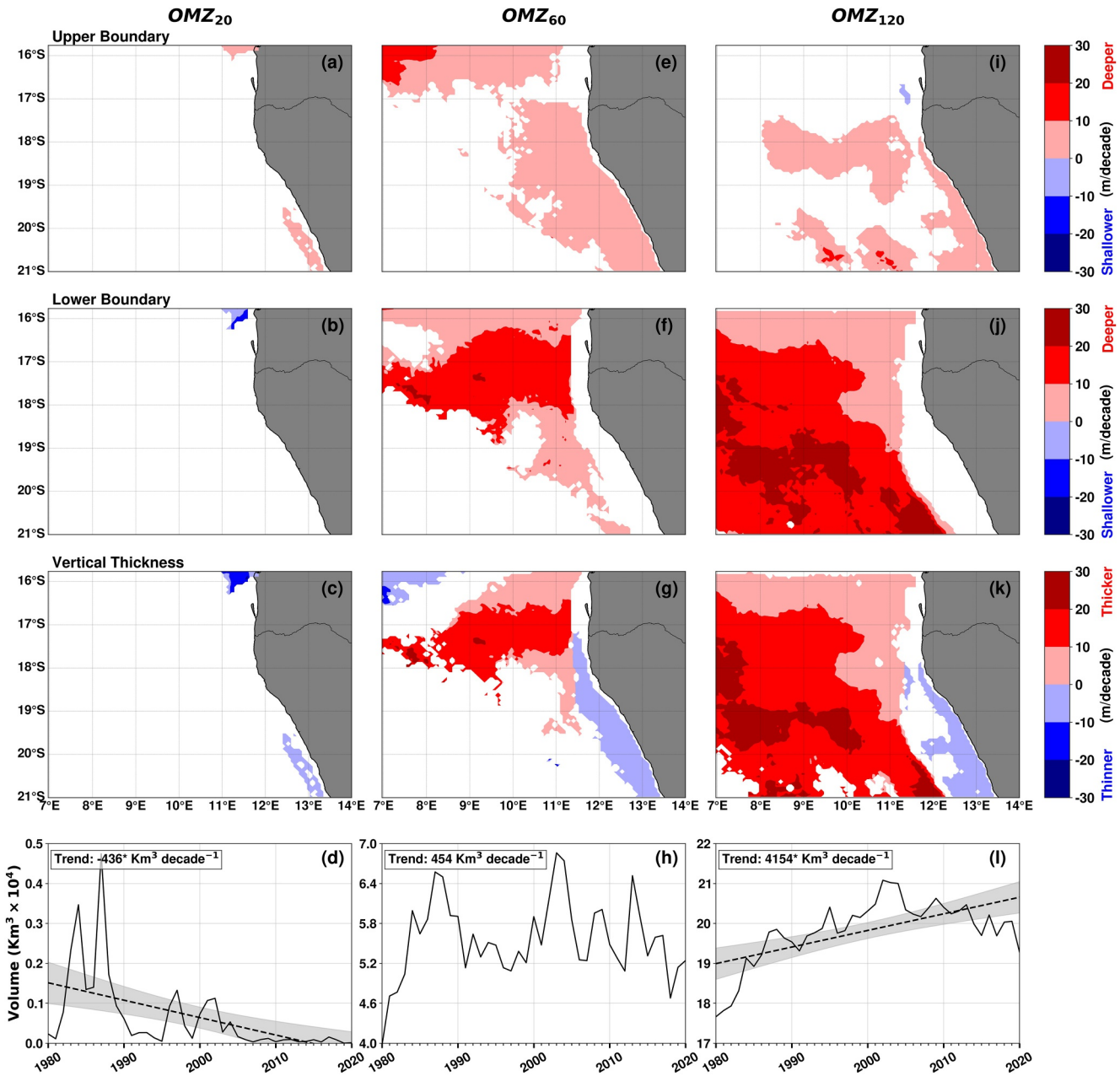

Figure 9. Trends of the selected Oxygen Minimum Zones (OMZ_{20}, OMZ_{60}, OMZ_{120}) boundaries and thickness in the NBUS over the period 1980–2020. The first three rows show the linear trends of the upper and lower OMZ boundaries and the vertical thickness, respectively. Specifically, panels (a–c), (e–g), and (i–k) show the upper boundary, lower boundary, and vertical thickness trends for OMZ_{20}, OMZ_{60}, and OMZ_{120}, respectively. Positive (red) and negative (blue) trends indicate deepening/shallowing or thickening/thinning. White areas denote statistically non-significant trends (p-value > 0.05). The bottom row panels (d, h, and l) illustrate the time evolution for each OMZ of total volume (solid line) and the associated linear trend (dashed line). The gray shading represents the 95% confidence interval. Asterisks indicate statistically significant trends at p-value < 0.05.

(Figure 9g). However, thinning is also evident over the continental shelf and northwestern regions, where shoaling values reach up to 10 m per decade. Despite this spatial variability, OMZ_{60} volume does not show a statistically significant long-term trend (Figure 9h).

The most pronounced and consistent trends are observed for the OMZ_{120} (Figures 9i–9l). The lower boundary shows strong deepening in open ocean areas, with values up to 28 m per decade (Figure 9j), while the upper boundary exhibits weaker deepening, reaching up to 13 m per decade (Figure 9i). These vertical shifts result in clear thickening of the OMZ_{120} layer, with trends approaching 30 m per decade, increasing progressively from the

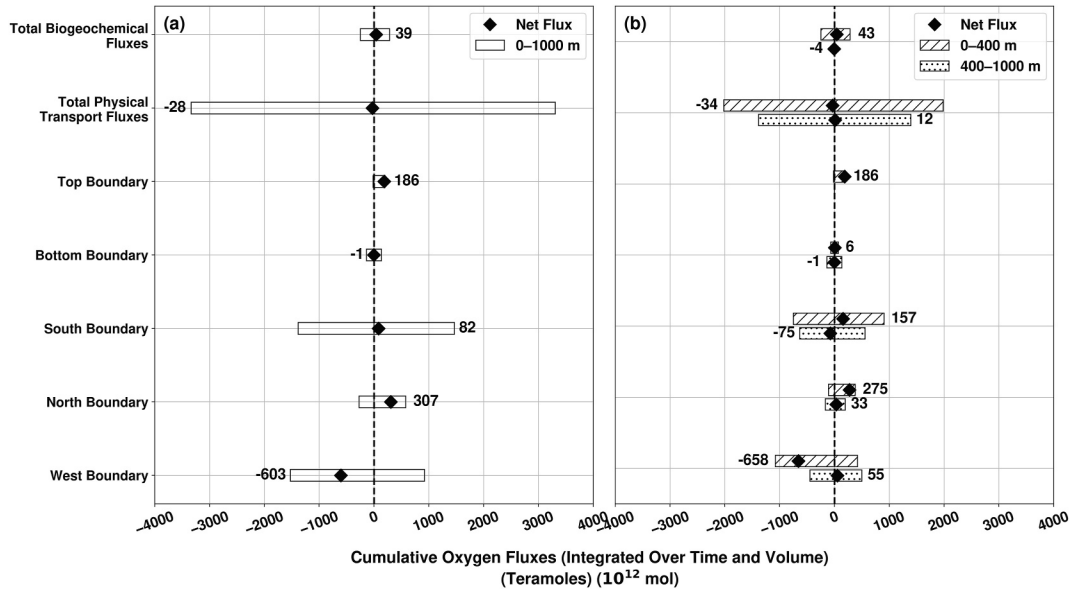

Figure 10. Cumulative DO fluxes (Tmol) representing the temporal sum over January 1980–December 2020 (see Section 2.6 for the budget's calculation), spatially and vertically integrated over the entire water column (a) (0–1,000 m; unfilled bars) and for two depth layers 0–400 m (hatched bars) and 400–1,000 m (dotted bars) (b). Fluxes are shown for the lateral boundaries (West, South, North), the bottom boundary (vertical fluxes at 400 and 1,000 m, respectively), and the top boundary (air–sea oxygen flux), along with the total biogeochemical fluxes, where positive values represent sources due to GPP and negative values represent sinks from community respiration. Black diamonds denote the net flux (with numbers representing the net flux values), and the vertical dashed line marks the zero value.

coast to the offshore domain (Figure 9k). A weak thinning trend is also present in the shallow coastal zone between 18°S and 21°S. Consistent with this vertical expansion, OMZ_{120} volume shows a statistically significant increase of +4,154 km^3 per decade (Figure 9l) (corresponding to a ∼2.1% increase per decade relative to its climatological mean), reflecting the broadening of low-oxygen conditions in the NBUS.

3.5. Dissolved Oxygen Budget in the NBUS

The estimated DO budget for the 0–1,000 m layer over the period 1980–2020 (Figure 10a) indicates a total oxygen input of 3,593 Tmol, of which 3,306 Tmol is supplied by lateral boundaries and 287 Tmol by GPP. Considering the relative contributions to the total input, the southern boundary was the largest source (40.8%), followed by the west (25.6%) and the north (16.1%) boundaries. Total oxygen loss was equal to 3,583 Tmol, slightly lower than the total input, thus resulting in an almost balanced budget within the whole NBUS domain. The most significant loss occurred at the west boundary (42.5%), followed by the southern (38.6%) and northern (7.6%) ones. At the bottom boundary, the input was nearly balancing the output, while the surface air-sea exchanges at the top boundary showed a clear net oxygen gain, with a relatively minor outgassing (0.4%).

Overall, the total net DO flux across physical boundaries over the four decades was −28 Tmol, indicating a net physical oxygen export from the NBUS domain. This export was offset by a net biogeochemical oxygen gain of +39 Tmol, arising from GPP (+287 Tmol) minus community respiration (−248 Tmol), yielding a combined physical–biogeochemical net flux of approximately +11 Tmol. This residual is small relative to the total oxygen input (3,593 Tmol) and output (3,583 Tmol), reflecting an almost closed oxygen budget, but it illustrates that biological oxygen production contributes to offsetting the net physical export.

The oxygen budget was also partitioned into an upper 0–400 m and a lower 400–1,000 m layer (Figure 10b; hatched bars), following the dipole structure described in Section 3.2. The budget reveals distinct differences in both physical and biogeochemical fluxes over the two vertical layers. The upper layer exhibited strong dynamics, with total oxygen input of 2271 Tmol and total output of 2263 Tmol, resulting in a net gain of +8 Tmol. However, when considering only physical fluxes, the upper layer shows a net oxygen export of 34 Tmol. This physical loss

is compensated by net oxygen production from GPP, which provides an input of 287 Tmol, thereby limiting the net imbalance and leading to an overall oxygen gain in the upper NBUS.

In contrast, the lower layer recorded input and output physical cumulative flux values of 1,394 and 1,383 Tmol, respectively, resulting in a physical net flux of approximately +11 Tmol (Figure 10b; hatched bars). Biogeochemical processes were nearly absent below 400 m, with almost no GPP contribution and only 4 Tmol of oxygen consumed through community respiration, indicating minimal biological influence in the NBUS deeper layer.

Comparatively, oxygen input from the northern boundary in the upper layer was ∼2 times that of the lower layer (381 vs. 199 Tmol), and input from the southern boundary was 1.6 times higher (907 vs. 560 Tmol). West boundary input was quite close between layers (∼421 and 500 Tmol), but the export was 2.4 times greater in the upper layer (1,079 vs. 445 Tmol). At the bottom boundary, fluxes were higher in the lower layer but still balanced in both cases. Overall, these results highlight the vertical variability of oxygen dynamics in the NBUS, with biological activity and more dynamic circulation evident in the upper layer, driving both transport and internal oxygen production.

4. Discussion

4.1. Temporal Variability of DO Inventory

The upper 1,000 m DO inventory (Figure 2a) integrates variability from dynamically distinct layers and therefore represents the net outcome of upper-ocean oxygenation and intermediate-to-deep deoxygenation. This integration explains why the inventory exhibits pronounced temporal variation despite an overall long-term decline: a sharp decrease during the first ∼8 years, a pronounced decline in the early 2000s, and a partial increase after 2005 even under continued warming.

The strong inventory decline during the first decade is most consistently explained by a rapid bottom-layer OHC increase. Over the period 1980–1998, OHC increases, particularly below 200 m, and coincides with the most negative DO trends in the 200–1,000 m layers (Figures 5b–5d). This is further supported by the causal discovery results (Figure 7), where OHC exerts a direct negative causal influence on DO, especially in deep layers, consistent with enhanced oxygen loss in the deeper layer that contributes disproportionately to the integrated (0–1,000 m) inventory. A comparable co-occurrence is evident in the early 2000s, when an increase in OHC is accompanied by intensified DO decline across the intermediate-to-deep layers (Figures 5c and 5d), indicating that episodic subsurface warming can amplify inventory losses. The increase in the integrated inventory occurring after the year 2005 can be interpreted as a shift in the balance between subsurface oxygen loss and upper-ocean ventilation-driven variability. In this period, the OHC variability becomes comparatively more stable (Figure 5), while the strengthening of τ_y and deepening of MLD (Figure 4a) indicate a change toward enhanced ventilation conditions in the upper layers that promote oxygenation. Consistent with this interpretation, PCMCI attributes most of the short-lag (month-scale) DO variability in the 0–400 m layer to physical causal variables associated with mixing and wind forcing (MLD and τ_y; Figure 6). In addition, the simulated fraction of oxygen-poor SACW decreases most strongly during the last decade (Figure S4a in Supporting Information S1), indicating a reduced intrusion of low-oxygen waters and thereby further supporting the positive inventory tendency.

4.2. Dipole Structure of DO Trends

According to our results, DO trends in the NBUS are not uniform. Our results reveal a distinct dipole structure, with oxygenation in the upper ∼400 m and over the shelf, and deoxygenation in deeper layers (400–1,000 m) and offshore regions (Section 3.2). This pattern appears to be a distinctive feature of the NBUS and is supported by several studies. Stramma and Schmidtko (2021) identified the region near the NBUS (8°S–14°S, 4°E–12°E) as the only oceanic area with a long-term oxygenation trend in the upper 50–300 m from 1950 to 2018, reporting +0.3 mmol m^{-3} per decade and deoxygenation of −1 mmol m^{-3} per decade in the 300–700 m layer. Six and Mikolajewicz (2022), using a high-resolution model of the BUS, found oxygen increases of up to 6 mmol m^{-3} per decade in the layer between 200 and 400 m, peaking near 15°S and extending into the NBUS shelf, over the 1960–2009 period. This intermediate-depth oxygenation was also supported by observational data from Schmidtko et al. (2017). In bottom layers, Ito et al. (2017) reported a deoxygenation trend below 400 m in the vicinity of the NBUS over the 1958–2015 period. Our results, together with previous studies, underscore the NBUS as a uniquely structured system with vertically contrasting DO trends.

Our findings indicate that DO trends are more strongly influenced by AOU than by DO_{sat}, suggesting that changes in ocean circulation, mixing, and/or biogeochemical processes—rather than solubility effects alone—are the primary causal influences of the observed pattern. Notably, even though DO_{sat} declined in the upper 400 m (Section 3.2), this layer exhibited an oxygenation trend, reinforcing the idea that non-thermal processes dominate DO variability here.

The causal discovery analysis showed that in the oxygenated upper 400 m, the DO variability was primarily linked to physical causal variables, specifically to the MLD, TKE, τ_y, and the intrusion of SACW and ESACW water masses on short (1 month) time lags. In contrast, biogeochemical variables such as NPP and community respiration exhibited weaker causal influence on DO in this layer. While this does not diminish the biological role in oxygen dynamics, it highlights that physical processes dominate the short-term control of upper-layer DO variability in the NBUS.

The oxygenation trend in the upper layers appears primarily linked to wind-induced turbulent mixing and a concurrent weakening of stratification. This interpretation is supported by the positive TKE trends (Figure 3d) and the declining trend in the BVF (Figure 3f), both indicating a less stratified and more vigorously mixed upper ocean. These conditions likely result from the long-term intensification of τ_y over the NBUS, which showed a significant positive trend (Figure 4a). Wind-induced mixing promotes weaker stratification and a plausible deepening of the MLD (Kataoka et al., 2019; Pollard et al., 1973), also as found in the southern Benguela (Carlson et al., 2025; Rogerson et al., 2025). Rixen et al. (2021) reported that enhanced mixing increases DO concentrations, while periods of wind relaxation strengthen stratification and impede downward ventilation (Nelson & Hutchings, 1983). Similarly, Carlson et al. (2025) demonstrated that wind-driven deep mixing enhances ventilation in the St Helena Bay waters (32°S), whereas low-oxygen conditions emerge during wind relaxation. Notably, our τ_y trends are consistent with previous studies reporting significant wind-stress intensification in the BUS (Narayan et al., 2010; Patti et al., 2010; Sydeman et al., 2014).

Furthermore, our results reveal a declining trend in the SACW fraction (Figure 4b), indicating a reduced contribution of oxygen-poor SACW to the NBUS, which likely contributes to the oxygenation trend in the upper layers, as the inflow of low-oxygen source waters is decreasing. In contrast, the ESACW (oxygen-rich water) fraction exhibits comparatively weak temporal variability. Such a reduction in the SACW fraction could be attributed to the intensified meridional wind stress, as Boyd (1988) and Pitcher et al. (2021) mentioned that stronger alongshore winds can constrain the poleward undercurrent direction, thereby limiting the inflow of hypoxic SACW waters. This interpretation is further supported by the simulated meridional velocity trends, which show localized strengthening of both northward and southward components (Figures S6c and S6d in Supporting Information S1), suggesting changes in the circulation pathways and relative contribution of water masses entering the NBUS; such changes may alter the local T–S characteristics and thereby affect SACW and ESACW fractions. Additionally, stronger alongshore winds may enhance offshore transport, exporting primary producers and organic matter away from the coast and thereby reducing local community respiration and DO consumption (Cury & Roy, 1989), consistent with the obtained negative trends in NPP and community respiration (Figures 3g and 3h). This mechanism is further supported by the long-term trends in zonal offshore velocity and vertical velocity (Figures S6a and S6b in Supporting Information S1). These trends show intensified upward velocity over the shelf in the upper ∼200 m (Figure S6b in Supporting Information S1), together with a substantially stronger increase in offshore transport (Figure S6a in Supporting Information S1). This enhanced offshore transport promotes cross-shelf export, leading to negative NPP and community respiration trends over the shelf and positive trends offshore.

Collectively, these findings indicate that the strengthening of upwelling-favorable winds has enhanced turbulent mixing and vertical ventilation, driving the recent oxygenation observed in the upper NBUS.

The budget analysis further illustrated how the NBUS upper layer is highly dynamic when considering the lateral oxygen fluxes, as it receives a higher amount of DO relative to the deeper one, primarily due to the influence of major current systems that dominate in upper layers (Figure 1a). These mesoscale circulation features enhance lateral mixing and facilitate oxygen supply in the upper ocean (Brandt et al., 2015; Frenger et al., 2018; Lovecchio et al., 2022; Six & Mikolajewicz, 2022). Fluctuations in current strength and position modulate DO concentrations, as physical fluxes may either increase or decrease local oxygen depending on their source (Lovecchio

et al., 2022). Thus, the oxygenation trend might be linked to changes in the intensity of the currents transporting oxygen-rich waters into the system, as indicated by the oxygen budget analysis (Figure 10b).

In the 400–1,000 m layer of the NBUS, the causal discovery application identified BVF and OHC as the primary causal factors of DO variability. This supports the notion that the vertical separation between the oxygenated upper layer and the deoxygenated lower layer is mainly governed by enhanced intermediate-layer stratification and warming-induced changes. As shown in (Figure 3f), the BVF exhibits a positive trend between 250 and 600 m, indicating increased stratification that inhibits vertical exchange, limits ventilation, and effectively impedes the downward transport of oxygen (see Bopp et al., 2002; Gnanadesikan et al., 2007; Plattner et al., 2002; Schmidtko et al., 2017). While this increase in stratification is consistent with the warming, it may also reflect changes in the density structure associated with a plausible lateral advection of water masses. In parallel, OHC shows a consistent positive trend across the water column, with its correlation to DO significantly stronger in the 400–1,000 m layers than in the upper ones (Figure 5). This suggests that DO concentrations at depth are particularly sensitive to heat content changes.

The positive OHC trends found in the subsurface layers of the NBUS (200–1,000 m) can likely be linked to changes in the properties of water masses supplying the Northern Benguela region, particularly enhanced Agulhas leakage and warming AAIW. Agulhas leakage advects relatively warm Indian Ocean waters into the Benguela Current thermocline and intermediate layers (upper ∼1,000 m) (Gordon et al., 1992; P. Richardson & Garzoli, 2003; P. L. Richardson, 2007). Observational and modeling studies indicate that Agulhas leakage has intensified since the 1980s due to changes in wind forcing (Biastoch et al., 2009; Rouault et al., 2009). In addition, AAIW forms a major subsurface component of the Benguela Current, entering the BUS at depths between 300 and 800 m (McKay et al., 2016). AAIW has experienced a multidecadal warming trend since the 1970s (Schmidtko & Johnson, 2012; Yang & He, 2014). Together, the intensified Agulhas leakage and the warming of AAIW at intermediate depths likely contribute to the observed increase in subsurface OHC in the NBUS, consistent with the agreement between simulated OHC trends and ARMOR3D observational estimates (Figure S5 in Supporting Information S1).

Our results, which indicate a significantly stronger correlation between OHC and DO in the bottom layers than in the surface layers, are consistent with the findings of Ito et al. (2017), who reported a deoxygenation trend below 400 m in the vicinity of the NBUS over the period 1958–2015, and found that the relationship between DO content and OHC becomes stronger with depth. This study suggests that oxygen inventory below the thermocline is particularly responsive to changes in heat content. Additionally, our oxygen budget analysis (Section 3.5) confirms sluggish circulation in bottom waters, with relatively lower lateral oxygen transport compared to the upper layer. Although the net physical bottom boundary oxygen flux in the 0–400 m layer was positive, it represented only a small oxygen supply to the NBUS bottom layer. Overall, deoxygenation in the deeper layer can be attributed to enhanced stratification, increased OHC, and weak circulation.

4.3. Diverging Trends in OMZs

The OMZ_{60} and OMZ_{120} in the NBUS exhibit a consistent deepening trend, reflected in their upper and lower boundaries, in addition to a thickening of their vertical extent—particularly beyond the continental shelf (Figure 9). This deepening corresponds to deoxygenation in bottom waters, which likely caused more water masses to fall below the OMZ_{60} and OMZ_{120} thresholds. In contrast, both OMZs show slight thinning in their vertical extent over the continental shelf, likely attributed to an oxygenation in the upper layers that elevates oxygen levels above critical thresholds. The vertical thickening of OMZ_{60}, more evident in open waters, is consistent with the findings of Stramma et al. (2008), which reported similar changes for OMZ_{60} in the vicinity of the NBUS over the period 1960–2018. Nevertheless, despite such deepening, its total volume doesn't exhibit a statistically significant trend (Figure 9h), likely due to regional variability: offshore expansion is offset by vertical thinning over the shelf, resulting in high interannual variability that masks long-term volume trends.

Conversely, the OMZ core (OMZ_{20})—located within the upper 300 m, does not show an expansion trend but instead shows limited contraction in a few locations (Figures 9a–9c). This OMZ core is shaped primarily by local turbulent mixing and biological respiration (Busecke et al., 2022; Lévy et al., 2022). The contraction likely results from a combination of increased oxygen in upper layers and a decline in local O_2 consumption, as indicated also by the negative trends in community respiration. Previous studies (e.g., Bahl et al., 2019; Busecke et al., 2022; Gnanadesikan et al., 2007) suggest that the expansion of OMZ_{120} is attributed to reduced ventilation in bottom

layers. These mechanisms are reflected in the simulated volume trends: OMZ_{120} shows a statistically significant increase in total volume, while OMZ_{20} contracts, due to the dipole structure discussed in the previous Section 4.2. The contrasting behavior of OMZ_{60} and OMZ_{120} expansion alongside OMZ_{20} contraction aligns with findings reported for the Pacific (Busecke et al., 2022) and the Indian Oceans (Ditkovsky et al., 2023).

4.4. Implications of OMZ_{60} and OMZ_{120} Deepening

The combined expansion and deepening of OMZ_{60} and OMZ_{120}, along with 400–1,000 m deoxygenation, is expected to have detrimental biogeochemical consequences in the NBUS. The expansion of low-oxygen water masses threatens the habitat, diversity, and survival of marine life (Busecke et al., 2022; Hamukuaya et al., 1998; Levin, 2018). Pelagic fish species with high oxygen demands, such as billfishes and tuna, are particularly vulnerable to the OMZ_{120} expansion, as they have tolerance thresholds near 150 mmol m^{-3} (Stramma et al., 2012). These species are abundant in the NBUS and support economically important fisheries (Hampton et al., 1999). Demersal fish in the NBUS, like deep-water hake and orange roughy, which typically inhabit depths below 400 m, are at increasing risk as deoxygenation intensifies in these deep layers. Other species, such as horse mackerel, which migrate to deeper zones as they mature, may also face compressed habitat (Hampton et al., 1999). Deoxygenation in the 400–1,000 m layer, along with the OMZ_{60} deepening, further impact the macro-benthic communities of the NBUS (Brodie Rudolph et al., 2020), especially over outer shelf regions. As oxygen levels decline, benthic diversity drops due to the loss of intolerant taxa and the proliferation of low-oxygen-adapted organisms (Currie et al., 2018; Hashim et al., 2024).

Moreover, the persistent decline in bottom-layer DO may progressively push oxygen levels toward thresholds at which denitrification becomes active (Knowles, 1982; Tyrrell & Lucas, 2002), resulting in increased nitrogen loss compared to phosphate retention (Nagel et al., 2013). This imbalance promotes phosphate efflux from sediments over the continental slope and reduces the NO_3^-/PO_4^{3-} ratio in upwelled waters, potentially shifting phytoplankton community composition and productivity (Schmidt & Eggert, 2016). In addition to the change in nutrient ratios caused by denitrification, very low oxygen conditions may also enhance the release of phosphate from authigenic sediments (Flynn et al., 2020). Continuous deoxygenation and severe oxygen loss in bottom waters stimulate microbial transformations that elevate nitrous oxide (N_2O) production via partial denitrification. As a potent greenhouse gas, increased N_2O emissions represent an additional consequence of deoxygenation (Farias & de la Maza, 2024; Frame et al., 2014; Wallschuss et al., 2025).

4.5. Methodological Considerations

A few aspects should be considered when interpreting the present results and in guiding future work. First, although DO consumption associated with the remineralization of sedimentary organic matter is included in the adopted pelagic–benthic closure and therefore represented in the model dynamics, the corresponding oxygen flux at the sediment–water interface was not saved as a separate diagnostic term for the budget. In addition, benthic processes other than remineralization that are not explicitly resolved by the simplified closure may limit the reconstruction of a fully closed DO budget. Second, the oxygen budget is reconstructed from monthly mean output. As a consequence, sub-monthly covariance between velocity and tracer fields is smoothed, which may introduce small errors in the diagnosed flux balance. Finally, while the analysis includes within-domain water-mass and circulation variables, the model configuration does not allow a full characterization of remote influences from water masses formed outside the NBUS. A more complete assessment of these larger-scale controls would require a broader spatial framework and dedicated water-mass tracking in future studies. Such future work should also include inter-comparisons with additional physical ocean models to further assess the robustness of the diagnosed water-mass fraction trends.

5. Conclusions

The Northern Benguela upwelling system is a distinct low-oxygen region, marked by persistent hypoxic and low-oxygen conditions. By exploiting the data from a highly resolved coupled physical–biogeochemical model, this work assessed long-term oxygen dynamics over the last four decades (1980–2020). The NBUS has lost a total of ∼1 Tmol of dissolved oxygen inventory in the upper 1,000 m during the considered period. A striking vertical dipole structure in the temporal evolution of dissolved oxygen within the NBUS emerged from the analyses, where the upper 400 m showed a net DO increase (0.3 Tmol), while the lower layer (400–1,000 m) contributed the

bulk of the loss, with 1.3 Tmol. This pattern reflects fundamentally different mechanisms: oxygenation in the upper layer was associated with enhanced wind-induced turbulent and vertical mixing and a declining fraction of the oxygen-poor South Atlantic Central Water, while bottom-layer deoxygenation was linked primarily to rising ocean heat content and increasing stratification that inhibits vertical mixing, with the subsurface warming likely influenced by changes in intermediate water masses entering the NBUS domain.

The oxygen budget reveals that 92% of oxygen fluxes in the NBUS are transported laterally via physical advection, while only 8% are attributable to internal biogeochemical production and lower-trophic-level respiration. This underscores the dominant role of physical circulation in shaping oxygen variability. Vertically, the upper 400 m show stronger boundary exchange, with oxygen exchange rates nearly twice those of the deeper layers. This is supported by active mesoscale circulation that enhances lateral mixing and facilitates oxygen supply. In contrast, the deeper layers are characterized by sluggish circulation and relatively weaker boundary oxygen transport. The evolving structure of oxygen minimum zones in the NBUS reflects these vertical oxygen trends: OMZ_{60} and OMZ_{120} have deepened by values reaching 120 m, while the OMZ core (OMZ_{20}), located within the increasingly oxygenated upper layers, has contracted. The most concerning implications of the revealed DO decline arise within the 400–1,000 m layer, where persistent deoxygenation may further constrain fish habitats, enhance microbially mediated N_2O production, and alter mid-depth biogeochemical cycling. In addition, localized deoxygenation over the outer continental shelf may increase stress on benthic communities.

Conflict of Interest

The authors declare no conflicts of interest relevant to this study.

Availability Statement

All model outputs and Python scripts used to perform the analyses in this study are openly available on Zenodo (Salama et al., 2026; https://doi.org/10.5281/zenodo.21069384). The repository, licensed under CC BY 4.0 (Creative Commons Attribution 4.0 International), includes the full set of NEMO and BFM NetCDF output files for the Northern Benguela Upwelling System, as well as the Jupyter Notebook containing all Python code used to generate the figures and analyses presented in this manuscript.

Acknowledgments

Thanks to the "CMCC Foundation—Euro-Mediterranean Center on Climate Change, Bologna, Italy" (CMCC) for providing access to the high-performance computing system (JUNO), which was instrumental in supporting the computational components of this research. I also gratefully acknowledge the National Oceanography Centre (NOC), Southampton, United Kingdom, for hosting me during a 3-month research stay and for providing an intellectually stimulating environment and access to essential resources that significantly advanced this work. *AS* and *TL* acknowledge funding from the European Union's Horizon 2020 Research and Innovation Programme under grant agreement no. 862923 (AtlantECO). *MB* acknowledges funding from the European Union under grant agreement 101083922 (OceanICU). *EL* and *SH* acknowledge funding by the European Research Council Consolidator Grant (GOCART, agreement number 724416). Views and opinions expressed are, however, those of the author (s) only and do not necessarily reflect those of the European Union or European Research Executive Agency. Neither the European Union nor the granting authority can be held responsible for them.

References

Abrahams, A., Schlegel, R. W., & Smit, A. J. (2021). A novel approach to quantify metrics of upwelling intensity, frequency, and duration. *PLoS One*, *16*(7), e0254026. https://doi.org/10.1371/journal.pone.0254026

Arévalo-Martínez, D. L., Steinhoff, T., Brandt, P., Körtzinger, A., Lamont, T., Rehder, G., & Bange, H. W. (2019). N2o emissions from the northern Benguela Upwelling System. *Geophysical Research Letters*, *46*(6), 3317–3326. https://doi.org/10.1029/2018GL081648

Bahl, A., Gnanadesikan, A., & Pradal, M.-A. (2019). Variations in ocean deoxygenation across Earth system models: Isolating the role of parameterized lateral mixing. *Global Biogeochemical Cycles*, *33*(6), 703–724. https://doi.org/10.1029/2018GB006121

Bakun, A. (1990). Global climate change and intensification of coastal ocean upwelling. *Science*, *247*(4939), 198–201. https://doi.org/10.1126/science.247.4939.198

Bakun, A., Black, B. A., Bograd, S. J., Garcia-Reyes, M., Miller, A. J., Rykaczewski, R. R., & Sydeman, W. J. (2015). Anticipated effects of climate change on coastal upwelling ecosystems. *Current Climate Change Reports*, *1*(2), 85–93. https://doi.org/10.1007/s40641-015-0008-4

Biastoch, A., Böning, C. W., Schwarzkopf, F. U., & Lutjeharms, J. (2009). Increase in Agulhas leakage due to poleward shift of southern hemisphere westerlies. *Nature*, *462*(7272), 495–498. https://doi.org/10.1038/nature08519

Bopp, L., Le Quéré, C., Heimann, M., Manning, A. C., & Monfray, P. (2002). Climate-induced oceanic oxygen fluxes: Implications for the contemporary carbon budget. *Global Biogeochemical Cycles*, *16*(2), 6-1–6-13. https://doi.org/10.1029/2001GB001445

Bordbar, M. H., Mohrholz, V., & Schmidt, M. (2023). Low confidence in multi-decadal trends of wind-driven upwelling across the Benguela Upwelling System. *Earth System Dynamics*, *14*(5), 1065–1080. https://doi.org/10.5194/esd-14-1065-2023

Boyd, A. J. (1988). *The oceanography of the Namibian shelf* (PhD thesis, p. 190). University of Cape Town.

Brandt, P., Bange, H. W., Banyte, D., Dengler, M., Didwischus, S.-H., Fischer, T., et al. (2015). On the role of circulation and mixing in the ventilation of oxygen minimum zones with a focus on the eastern tropical north Atlantic. *Biogeosciences*, *12*(2), 489–512. https://doi.org/10.5194/bg-12-489-2015

Brandt, P., Bordbar, M. H., Coelho, P., Koungue, R. A. I., Körner, M., Lamont, T., et al. (2024). Physical drivers of southwest African coastal upwelling and its response to climate variability and change. In G. P. von Maltitz, et al. (Eds.), *Sustainability of southern African ecosystems under global change: Science for management and policy interventions* (pp. 221–257). Springer International Publishing. https://doi.org/10.1007/978-3-031-10948-5_9

Breitburg, D., Levin, L. A., Oschlies, A., Grégoire, M., Chavez, F. P., Conley, D. J., et al. (2018). Declining oxygen in the global ocean and coastal waters. *Science*, *359*(6371), eaam7240. https://doi.org/10.1126/science.aam7240

Brodie Rudolph, T., Ruckelshaus, M., Swilling, M., Allison, E. H., Österblom, H., Gelcich, S., & Mbatha, P. (2020). A transition to sustainable ocean governance. *Nature Communications*, *11*(1), 3600. https://doi.org/10.1038/s41467-020-17410-2

Busecke, J. J., Resplandy, L., Ditkovsky, S. J., & John, J. G. (2022). Diverging fates of the Pacific Ocean oxygen minimum zone and its core in a warming world. *AGU Advances*, *3*(6), e2021AV000470. https://doi.org/10.1029/2021AV000470

Carlson, A., Siedlecki, S., Granger, J., Veitch, J., Pitcher, G., Fearon, G., et al. (2025). Seasonal source water changes and winds contribute to the development of hypoxia in St Helena Bay within the southern Benguela Upwelling System. *Journal of Geophysical Research: Oceans*, *130*(4), e2024JC021702. https://doi.org/10.1029/2024JC021702

Carr, M.-E. (2001). Estimation of potential productivity in eastern boundary currents using remote sensing. *Deep Sea Research Part II: Topical Studies in Oceanography*, *49*(1–3), 59–80. https://doi.org/10.1016/S0967-0645(01)00094-7

CMEMS. (2022). *Multi observation global ocean 3d temperature salinity height geostrophic current and MLD*. E.U. Copernicus Marine Service Information (CMEMS). Marine Data Store (MDS). https://doi.org/10.48670/moi-00052

Cooley, S., Schoeman, D., Bopp, L., Boyd, P., Donner, D., Ghebrehiwet, S., et al. (2022). Oceans and coastal ecosystems and their services. In *IPCC AR6 WGII*. Cambridge University Press. https://doi.org/10.1017/9781009325844.005

Currie, B., Utne-Palm, A. C., & Salvanes, A. G. V. (2018). Winning ways with hydrogen sulphide on the Namibian Shelf. *Frontiers in Marine Science*, *5*, 341. https://doi.org/10.3389/fmars.2018.00341

Cury, P., & Roy, C. (1989). Optimal environmental window and pelagic fish recruitment success in upwelling areas. *Canadian Journal of Fisheries and Aquatic Sciences*, *46*(4), 670–680. https://doi.org/10.1139/f89-086

De Szoeke, R., & Richman, J. (1981). The role of wind-generated mixing in coastal upwelling. *Journal of Physical Oceanography*, *11*(11), 1534–1547. https://doi.org/10.1175/1520-0485(1981)011<1534:TROWGM>2.0.CO;2

Ditkovsky, S., Resplandy, L., & Busecke, J. (2023). Unique ocean circulation pathways reshape the Indian Ocean oxygen minimum zone with warming. *Biogeosciences*, *20*(23), 4711–4736. https://doi.org/10.5194/bg-20-4711-2023

Ekau, W., Auel, H., Hagen, W., Koppelmann, R., Wasmund, N., Bohata, K., et al. (2018). Pelagic key species and mechanisms driving energy flows in the northern Benguela Upwelling Ecosystem and their feedback into biogeochemical cycles. *Journal of Marine Systems*, *188*, 49–62. https://doi.org/10.1016/j.jmarsys.2018.03.001

Emeis, K., Eggert, A., Flohr, A., Lahajnar, N., Nausch, G., Neumann, A., et al. (2018). Biogeochemical processes and turnover rates in the northern Benguela Upwelling System. *Journal of Marine Systems*, *188*, 63–80. https://doi.org/10.1016/j.jmarsys.2017.10.001

Farias, L., & de la Maza, L. (2024). Understanding the impacts of coastal deoxygenation in nitrogen dynamics: An observational analysis. *Scientific Reports*, *14*(1), 11826. https://doi.org/10.1038/s41598-024-62186-w

Flohr, A., Van Der Plas, A., Emeis, K.-C., Mohrholz, V., & Rixen, T. (2014). Spatio-temporal patterns of C: N: P ratios in the northern Benguela Upwelling System. *Biogeosciences*, *11*(3), 885–897. https://doi.org/10.5194/bg-11-885-2014

Flynn, R., Granger, J., Veitch, J., Siedlecki, S., Burger, J., Pillay, K., & Fawcett, S. (2020). On-shelf nutrient trapping enhances the fertility of the southern Benguela Upwelling System. *Journal of Geophysical Research: Oceans*, *125*(6), e2019JC015948. https://doi.org/10.1029/2019JC015948

Frame, C. H., Deal, E., Nevison, C. D., & Casciotti, K. L. (2014). N_2O production in the eastern south Atlantic: Analysis of N_2O stable isotopic and concentration data. *Global Biogeochemical Cycles*, *28*(11), 1262–1278. https://doi.org/10.1002/2013GB004790

Frenger, I., Bianchi, D., Stührenberg, C., Oschlies, A., Dunne, J., Deutsch, C., et al. (2018). Biogeochemical role of subsurface coherent eddies in the ocean: Tracer cannonballs, hypoxic storms, and microbial stewpots? *Global Biogeochemical Cycles*, *32*(2), 226–249. https://doi.org/10.1002/2017GB005743

Gammelsrød, T., Bartholomae, C., Boyer, D., Filipe, V., & O'toole, M. (1998). Intrusion of warm surface water along the Angolan Namibian Coast in February–March 1995: The 1995 Benguela Niño. *African Journal of Marine Science*, *19*(1), 41–56. https://doi.org/10.2989/025776198784126719

Garcia, H. E., Weathers, K. W., Paver, C. R., Smolyar, I. V., Boyer, T. P., Locarnini, R. A., et al. (2019). World ocean atlas 2018, volume 3: Dissolved oxygen, apparent oxygen utilization, and dissolved oxygen saturation. Retrieved from https://www.ncei.noaa.gov/data/oceans/woa/WOA18

García-Reyes, M., Sydeman, W. J., Schoeman, D. S., Rykaczewski, R. R., Black, B. A., Smit, A. J., & Bograd, S. J. (2015). Under pressure: Climate change, upwelling, and eastern boundary upwelling ecosystems. *Frontiers in Marine Science*, *2*, 109. https://doi.org/10.3389/fmars.2015.00109

Garçon, V., Dewitte, B., Montes, I., & Goubanova, K. (2019). Land-sea-atmosphere interactions exacerbating ocean deoxygenation in eastern boundary upwelling systems (ebus). In *Ocean Deoxygenation Everyone's Problem* (pp. 155–170). Retrieved from https://portals.iucn.org/library/sites/library/files/documents/03.4%20DEOX.pdf

Garzoli, S., & Gordon, A. (1996). Origins and variability of the Benguela Current. *Journal of Geophysical Research*, *101*(C1), 897–906. https://doi.org/10.1029/95JC03221

GEBCO Compilation Group. (2021). GEBCO 2021 Grid. https://doi.org/10.5285/c6612cbe-50b3-0cff-e053-6c86abc09f8f

Gilbert, D., Rabalais, N., Díaz, R., & Zhang, J. (2010). Evidence for greater oxygen decline rates in the coastal ocean than in the open ocean. *Biogeosciences*, *7*(7), 2283–2296. https://doi.org/10.5194/bg-7-2283-2010

Gnanadesikan, A., Russell, J., & Zeng, F. (2007). How does ocean ventilation change under global warming? *Ocean Science*, *3*(1), 43–53. https://doi.org/10.5194/os-3-43-2007

Gordon, A. L. (1981). South Atlantic thermocline ventilation. *Deep-Sea Research, Part A: Oceanographic Research Papers*, *28*(11), 1239–1264. https://doi.org/10.1016/0198-0149(81)90033-9

Gordon, A. L., Weiss, R. F., Smethie, W. M., Jr., & Warner, M. J. (1992). Thermocline and intermediate water communication between the south Atlantic and Indian Oceans. *Journal of Geophysical Research*, *97*(C5), 7223–7240. https://doi.org/10.1029/92JC00485

Guinehut, S., Dhomps, A.-L., Larnicol, G., & Le Traon, P.-Y. (2012). High resolution 3-d temperature and salinity fields derived from in situ and satellite observations. *Ocean Science*, *8*(5), 845–857. https://doi.org/10.5194/os-8-845-2012

Hagen, E., Feistel, R., Agenbag, J. J., & Ohde, T. (2001). Seasonal and interannual changes in intense Benguela Upwelling (1982–1999). *Oceanologica Acta*, *24*(6), 557–568. https://doi.org/10.1016/S0399-1784(01)01173-2

Hampton, I., Boyer, D., Penney, A., Pereira, A., & Sardinha, M. (1999). *Integrated overview of fisheries of the Benguela Current Region*. Synthesis and assessment of information on the Benguela Current Large Marine Ecosystem (BCLME). Retrieved from https://archive.iwlearn.net/bclme.org/factfig/fisheries.html

Hamukuaya, H., O'Toole, M., & Woodhead, P. (1998). Observations of severe hypoxia and offshore displacement of cape hake over the Namibian Shelf in 1994. *South African Journal of Marine Science*, *19*(1), 57–59. https://doi.org/10.2989/025776198784126809

Hashim, S. M., Waweru, B. W., & Muthumbi, A. (2024). Influence of oxygen minimum zone on macrobenthic community structure in the northern Benguela Upwelling System: A macro-nematode perspective. *Biogeosciences*, *21*(12), 2995–3006. https://doi.org/10.5194/bg-21-2995-2024

Hegglin, M. I., Kinnison, D., Lamarque, J.-F., & Plummer, D. (2016). *input4mips.cmip6.cmip.ureading*. Earth System Grid Federation. https://doi.org/10.22033/ESGF/input4MIPs.10452

Hersbach, H., Bell, B., Berrisford, P., Hirahara, S., Horányi, A., Muñoz-Sabater, J., et al. (2020). The ERA5 global reanalysis. *Quarterly Journal of the Royal Meteorological Society*, *146*(730), 1999–2049. https://doi.org/10.1002/qj.3803

Heymans, J. J., Shannon, L. J., & Jarre, A. (2004). Changes in the northern Benguela ecosystem over three decades: 1970s, 1980s, and 1990s. *Ecological Modelling*, *172*(2–4), 175–195. https://doi.org/10.1016/j.ecolmodel.2003.09.006

Hollitzer, H. A., Patara, L., Terhaar, J., & Oschlies, A. (2024). Competing effects of wind and buoyancy forcing on ocean oxygen trends in recent decades. *Nature Communications*, *15*(1), 9264. https://doi.org/10.1038/s41467-024-53557-y

Hutchings, L., Van der Lingen, C. D., Shannon, L. J., Crawford, R. J. M., Verheye, H. M. S., Bartholomae, C. H., et al. (2009). The Benguela Current: An ecosystem of four components. *Progress in Oceanography*, *83*(1–4), 15–32. https://doi.org/10.1016/j.pocean.2009.07.046

IOC, SCOR, & IAPSO. (2010). *The international thermodynamic equation of seawater–2010: Calculation and use of thermodynamic properties* (Intergovernmental Oceanographic Commission, UNESCO Manuals and Guides No. 56, p. 196). Retrieved from https://www.teos-10.org/pubs/TEOS-10_Manual.pdf

Ito, T., Garcia, H. E., Wang, Z., Minobe, S., Long, M. C., Cebrian, J., et al. (2024). Underestimation of multi-decadal global O_2 loss due to an optimal interpolation method. *Biogeosciences*, *21*(3), 747–759. https://doi.org/10.5194/bg-21-747-2024

Ito, T., Minobe, S., Long, M. C., & Deutsch, C. (2017). Upper ocean O_2 trends: 1958–2015. *Geophysical Research Letters*, *44*(9), 4214–4223. https://doi.org/10.1002/2017GL073613

Kainge, P., Kirkman, S. P., Estevão, V., van der Lingen, C. D., Uanivi, U., Kathena, J. N., et al. (2020). Fisheries yields, climate change, and ecosystem-based management of the Benguela current large marine ecosystem. *Environmental Development*, *36*, 100567. https://doi.org/10.1016/j.envdev.2020.100567

Kämpf, J., Chapman, P., Kämpf, J., & Chapman, P. (2016). The functioning of coastal upwelling systems. In *Upwelling systems of the world: A scientific journey to the most productive marine ecosystems* (pp. 31–65). https://doi.org/10.1007/978-3-319-42524-5

Kataoka, T., Kimoto, M., Watanabe, M., & Tatebe, H. (2019). Wind–mixed layer–SST feedbacks in a tropical air–sea coupled system: Application to the Atlantic. *Journal of Climate*, *32*(13), 3865–3881. https://doi.org/10.1175/JCLI-D-18-0728.1

Knowles, R. (1982). Denitrification. *Microbiological Reviews*, *46*(1), 43–70. https://doi.org/10.1128/mr.46.1.43-70.1982

Kopte, R., Brandt, P., Dengler, M., Tchipalanga, P., Macuéria, M., & Ostrowski, M. (2017). The Angola current: Flow and hydrographic characteristics as observed at 11°S. *Journal of Geophysical Research: Oceans*, *122*(2), 1177–1189. https://doi.org/10.1002/2016JC012374

Kwiatkowski, L., Torres, O., Bopp, L., Aumont, O., Chamberlain, M., Christian, J. R., et al. (2020). Twenty-first century ocean warming, acidification, deoxygenation, and upper-ocean nutrient and primary production decline from CMIP6 model projections. *Biogeosciences*, *17*(13), 3439–3470. https://doi.org/10.5194/bg-17-3439-2020

Lachkar, Z., Cornejo-D'Ottone, M., Singh, A., Arístegui, J., Dewitte, B., Fawcett, S., et al. (2024). Biogeochemistry of greenhouse gases in coastal upwelling systems: Processes and sensitivity to global change. *Elementa: Science of the Anthropocene*, *12*(1), 00088. https://doi.org/10.1525/elementa.2023.00088

Levin, L. A. (2018). Manifestation, drivers, and emergence of open ocean deoxygenation. *Annual Review of Marine Science*, *10*(1), 229–260. https://doi.org/10.1146/annurev-marine-121916-063359

Lévy, M., Resplandy, L., Palter, J. B., Couespel, D., & Lachkar, Z. (2022). The crucial contribution of mixing to present and future ocean oxygen distribution. In *Ocean mixing* (pp. 329–344). Elsevier. https://doi.org/10.1016/B978-0-12-821512-8.00020-7

Lovato, T., Peano, D., Butenschön, M., Materia, S., Iovino, D., Scoccimarro, E., et al. (2022). CMIP6 simulations with the CMCC Earth system model (CMCC-ESM2). *Journal of Advances in Modeling Earth Systems*, *14*(3), e2021MS002814. https://doi.org/10.1029/2021MS002814

Lovecchio, E., Henson, S., Carvalho, F., & Briggs, N. (2022). Oxygen variability in the offshore northern Benguela upwelling system from glider data. *Journal of Geophysical Research: Oceans*, *127*(11), e2022JC019063. https://doi.org/10.1029/2022JC019063

Lovecchio, E., Henson, S., Carvalho, F., Briggs, N., Hilder, H., Wolff, G. A., et al. (2025). Mesopelagic particle layers in the dynamic hypoxic northern Benguela are shaped by zooplankton activity. *Journal of Geophysical Research: Oceans*, *130*(3), e2024JC021039. https://doi.org/10.1029/2024JC021039

Madec, G., & the NEMO System Team. (2023). Nemo ocean engine reference manual [Computer software manual]. https://doi.org/10.5281/zenodo.8167700

McKay, C., Filipsson, H. L., Romero, O. E., Stuut, J.-B., & Björck, S. (2016). The interplay between the surface and bottom water environment within the Benguela Upwelling System over the last 70 ka. *Paleoceanography*, *31*(2), 266–285. https://doi.org/10.1002/2015PA002792

Meiritz, L. C., Rixen, T., van der Plas, A. K., Lamont, T., & Lahajnar, N. (2024). The influence of zooplankton and oxygen on the particulate organic carbon flux in the Benguela Upwelling System. *Biogeosciences*, *21*(22), 5261–5276. https://doi.org/10.5194/egusphere-2024-700

Messié, M., Ledesma, J., Kolber, D. D., Michisaki, R. P., Foley, D. G., & Chavez, F. P. (2009). Potential new production estimates in four eastern boundary upwelling ecosystems. *Progress in Oceanography*, *83*(1–4), 151–158. https://doi.org/10.1016/j.pocean.2009.07.018

Mohn, C., Schwarzkopf, F. U., Jiménez García, P., Orejas, C., Huvenne, V. A. I., Schumacher, M., et al. (2025). Dynamics of near-bottom currents in cold-water coral and sponge areas at Valdivia Bank and Ewing Seamount, southeast Atlantic. *Journal of Geophysical Research: Oceans*, *130*(1), e2024JC021667. https://doi.org/10.1029/2024JC021667

Mohrholz, V., Bartholomae, C., Van der Plas, A., & Lass, H. (2008). The seasonal variability of the northern Benguela undercurrent and its relation to the oxygen budget on the shelf. *Continental Shelf Research*, *28*(3), 424–441. https://doi.org/10.1016/j.csr.2007.10.001

Mohrholz, V., Eggert, A., Junker, T., Nausch, G., Ohde, T., & Schmidt, M. (2014). Cross shelf hydrographic and hydrochemical conditions and their short term variability at the northern Benguela during a normal upwelling season. *Journal of Marine Systems*, *140*, 92–110. https://doi.org/10.1016/j.jmarsys.2014.04.019

Monteiro, P. M., & van der Plas, A. K. (2006). 5 low oxygen water (low) variability in the Benguela system: Key processes and forcing scales relevant to forecasting. In *Large marine ecosystems* (Vol. 14, pp. 71–90). Elsevier. https://doi.org/10.1016/S1570-0461(06)80010-8

Nagel, B., Emeis, K.-C., Flohr, A., Rixen, T., Schlarbaum, T., Mohrholz, V., & van der Plas, A. (2013). N-cycling and balancing of the n-deficit generated in the oxygen minimum zone over the Namibian Shelf—An isotope-based approach. *Journal of Geophysical Research: Biogeosciences*, *118*(1), 361–371. https://doi.org/10.1002/jgrg.20040

Narayan, N., Paul, A., Mulitza, S., & Schulz, M. (2010). Trends in coastal upwelling intensity during the late 20th century. *Ocean Science*, *6*(3), 815–823. https://doi.org/10.5194/os-6-815-2010

Nelson, G., & Hutchings, L. (1983). The Benguela upwelling area. *Progress in Oceanography*, *12*(3), 333–356. https://doi.org/10.1016/0079-6611(83)90013-7

Ohde, T., & Dadou, I. (2018). Seasonal and annual variability of coastal sulphur plumes in the northern Benguela Upwelling System. *PLoS One*, *13*(2), e0192140. https://doi.org/10.1371/journal.pone.0192140

Orr, J. C., Najjar, R. G., Aumont, O., Bopp, L., Bullister, J. L., Danabasoglu, G., et al. (2017). Biogeochemical protocols and diagnostics for the CMIP6 ocean model intercomparison project (OMIP). *Geoscientific Model Development*, *10*(6), 2169–2199. https://doi.org/10.5194/gmd-10-2169-2017

Patti, B., Guisande, C., Riveiro, I., Thejll, P., Cuttitta, A., Bonanno, A., et al. (2010). Effect of atmospheric CO_2 and solar activity on wind regime and water column stability in the major global upwelling areas. Estuarine. *Coastal and Shelf Science*, *88*(1), 45–52. https://doi.org/10.1016/j.ecss.2010.03.004

Pitcher, G. C., Aguirre-Velarde, A., Breitburg, D., Cardich, J., Carstensen, J., Conley, D. J., et al. (2021). System controls of coastal and open ocean oxygen depletion. *Progress in Oceanography*, *197*, 102613. https://doi.org/10.1016/j.pocean.2021.102613

Plattner, G.-K., Joos, F., & Stocker, T. F. (2002). Revision of the global carbon budget due to changing air-sea oxygen fluxes. *Global Biogeochemical Cycles*, *16*(4), 43-1–43-12. https://doi.org/10.1029/2001GB001746

Pollard, R. T., Rhines, P. B., & Thompson, R. O. (1973). The deepening of the wind-mixed layer. *Geophysical Fluid Dynamics*, *4*(4), 381–404. https://doi.org/10.1080/03091927208236105

Poole, R., & Tomczak, M. (1999). Optimum multiparameter analysis of the water mass structure in the Atlantic Ocean thermocline. *Deep Sea Research Part I: Oceanographic Research Papers*, *46*(11), 1895–1921. https://doi.org/10.1016/S0967-0637(99)00025-4

Richardson, P., & Garzoli, S. (2003). Characteristics of intermediate water flow in the Benguela current as measured with rafos floats. *Deep Sea Research Part II: Topical Studies in Oceanography*, *50*(1), 87–118. https://doi.org/10.1016/S0967-0645(02)00380-6

Richardson, P. L. (2007). Agulhas leakage into the Atlantic estimated with subsurface floats and surface drifters. *Deep Sea Research Part I: Oceanographic Research Papers*, *54*(8), 1361–1389. https://doi.org/10.1016/j.dsr.2007.04.010

Rimaud, J., Speich, S., Blanke, B., & Grima, N. (2012). The exchange of intermediate water in the southeast Atlantic: Water mass transformations diagnosed from the Lagrangian analysis of a regional ocean model. *Journal of Geophysical Research*, *117*(C8). https://doi.org/10.1029/2012JC008059

Rixen, T., Lahajnar, N., Lamont, T., Koppelmann, R., Martin, B., Van Beusekom, J. E., et al. (2021). Oxygen and nutrient trapping in the southern Benguela Upwelling System. *Frontiers in Marine Science*, *8*, 730591. https://doi.org/10.3389/fmars.2021.730591

Rogerson, J., Veitch, J., Siedlecki, S., & Fawcett, S. (2025). Frontal features and mixing regimes along the shelf region of the southern Benguela Upwelling System. *Continental Shelf Research*, *295*, 105560. https://doi.org/10.1016/j.csr.2025.105560

Rouault, M., Penven, P., & Pohl, B. (2009). Warming in the Agulhas Current System since the 1980's. *Geophysical Research Letters*, *36*(12). https://doi.org/10.1029/2009GL037987

Runge, J., Gerhardus, A., Varando, G., Eyring, V., & Camps-Valls, G. (2023). Causal inference for time series. *Nature Reviews Earth & Environment*, *4*(7), 487–505. https://doi.org/10.1038/s43017-023-00431-y

Runge, J., Nowack, P., Kretschmer, M., Flaxman, S., & Sejdinovic, D. (2019). Detecting and quantifying causal associations in large nonlinear time series datasets. *Science Advances*, *5*(11), eaau4996. https://doi.org/10.1126/sciadv.aau4996

Sabbaghzadeh, B., Arévalo-Martínez, D. L., Glockzin, M., Otto, S., & Rehder, G. (2021). Meridional and cross-shelf variability of N_2O and CH_4 in the eastern-south Atlantic. *Journal of Geophysical Research: Oceans*, *126*(11), e2020JC016878. https://doi.org/10.1029/2020JC016878

Salama, A. T., Lovato, T., Butenschön, M., & Zavatarelli, M. (2025). A coupled physical-biogeochemical modeling approach to investigate the dynamics of the Benguela Upwelling System. *Frontiers in Marine Science*, *12*, 1601284. https://doi.org/10.3389/fmars.2025.1601284

Salama, A. T., Lovato, T., Butenschön, M., & Zavatarelli, M. (2026). Physical and biogeochemical model data for the northern Benguela Upwelling System (1980–2020) [Dataset]. *Zenodo*. https://doi.org/10.5281/zenodo.21069384

Sarmiento, J. L., Gruber, N., Brzezinski, M., & Dunne, J. (2004). High-latitude controls of thermocline nutrients and low latitude biological productivity. *Nature*, *427*(6969), 56–60. https://doi.org/10.1038/nature02127

Schmidt, M., & Eggert, A. (2016). Oxygen cycling in the northern Benguela Upwelling System: Modelling oxygen sources and sinks. *Progress in Oceanography*, *149*, 145–173. https://doi.org/10.1016/j.pocean.2016.09.004

Schmidtko, S., & Johnson, G. C. (2012). Multidecadal warming and shoaling of Antarctic intermediate water. *Journal of Climate*, *25*(1), 207–221. https://doi.org/10.1175/JCLI-D-11-00021.1

Schmidtko, S., Stramma, L., & Visbeck, M. (2017). Decline in global oceanic oxygen content during the past five decades. *Nature*, *542*(7641), 335–339. https://doi.org/10.1038/nature21399

Shannon, L., & O'Toole, M. (1999). *Synthesis and assessment of information on the Benguela current large marine ecosystem (BCLME) thematic report no. 2: Integrated overview of the oceanography and environmental variability of the Benguela Current Region*. Submitted to the United Nations Development Programme. Retrieved from https://archive.iwlearn.net/bclme.org/factfig/oceanography.html

Sharp, J. D., Fassbender, A. J., Carter, B. R., Johnson, G. C., Schultz, C., & Dunne, J. P. (2023). GOBAI-O 2: Temporally and spatially resolved fields of ocean interior dissolved oxygen over nearly two decades. *Earth System Science Data Discussions*, *2023*, 1–46. https://doi.org/10.5194/essd-15-4481-2023

Siddiqui, C., Rixen, T., Lahajnar, N., Van der Plas, A. K., Louw, D. C., Lamont, T., & Pillay, K. (2023). Regional and global impact of CO_2 uptake in the Benguela Upwelling System through preformed nutrients. *Nature Communications*, *14*(1), 2582. https://doi.org/10.1038/s41467-023-38208-y

Siegfried, L., Schmidt, M., Mohrholz, V., Pogrzeba, H., Nardini, P., Böttinger, M., & Scheuermann, G. (2019). The tropical-subtropical coupling in the southeast Atlantic from the perspective of the northern Benguela Upwelling System. *PLoS One*, *14*(1), e0210083. https://doi.org/10.1371/journal.pone.0210083

Six, K. D., & Mikolajewicz, U. (2022). High-resolution modelling of long-term trends in the oxygen and carbon cycles of the Benguela Upwelling System. *Biogeosciences Discussions*, 1–51. https://doi.org/10.5194/bg-2022-27

Soetaert, K., Middelburg, J. J., Herman, P. M., & Buis, K. (2000). On the coupling of benthic and pelagic biogeochemical models. *Earth-Science Reviews*, *51*(1–4), 173–201. https://doi.org/10.1016/S0012-8252(00)00004-0

Stramma, L., Johnson, G. C., Sprintall, J., & Mohrholz, V. (2008). Expanding oxygen-minimum zones in the tropical oceans. *Science*, *320*(5876), 655–658. https://doi.org/10.1126/science.1153847

Stramma, L., & Peterson, R. G. (1990). The south Atlantic Current. *Journal of Physical Oceanography*, *20*(6), 846–859. https://doi.org/10.1175/1520-0485(1990)020<0846:TSAC>2.0.CO;2

Stramma, L., Prince, E. D., Schmidtko, S., Luo, J., Hoolihan, J. P., Visbeck, M., et al. (2012). Expansion of oxygen minimum zones may reduce available habitat for tropical pelagic fishes. *Nature Climate Change*, *2*(1), 33–37. https://doi.org/10.1038/nclimate1304

Stramma, L., & Schmidtko, S. (2021). Tropical deoxygenation sites revisited to investigate oxygen and nutrient trends. *Ocean Science*, *17*(3), 833–847. https://doi.org/10.5194/os-17-833-2021

Sydeman, W., García-Reyes, M., Schoeman, D. S. R., Thompson, S., Black, B., & Bograd, S. (2014). Climate change and wind intensification in coastal upwelling ecosystems. *Science*, *345*(6192), 77–80. https://doi.org/10.1126/science.1251635

Talley, L. D. (1996). Antarctic intermediate water in the south Atlantic. In *The south Atlantic*. Springer. https://doi.org/10.1007/978-3-642-80353-6_11

Tim, N., Zorita, E., Schwarzkopf, F. U., Rühs, S., Emeis, K.-C., & Biastoch, A. (2018). The impact of Agulhas leakage on the central water masses in the Benguela Upwelling System from a high-resolution ocean simulation. *Journal of Geophysical Research: Oceans*, *123*(12), 9416–9428. https://doi.org/10.1029/2018JC014218

Tyrrell, T., & Lucas, M. I. (2002). Geochemical evidence of denitrification in the Benguela upwelling system. *Continental Shelf Research*, *22*(17), 2497–2511. https://doi.org/10.1016/S0278-4343(02)00077-8

Veitch, J., Penven, P., & Shillington, F. (2009). The Benguela: A laboratory for comparative modeling studies. *Progress in Oceanography*, *83*(1–4), 296–302. https://doi.org/10.1016/j.pocean.2009.07.008

Veleda, D., Araujo, M., Zantopp, R., & Montagne, R. (2012). Intraseasonal variability of the north Brazil undercurrent forced by remote winds. *Journal of Geophysical Research*, *117*(C11). https://doi.org/10.1029/2012JC008392

Verheye, H. M., Lamont, T., Huggett, J. A., Kreiner, A., & Hampton, I. (2016). Plankton productivity of the Benguela current large marine ecosystem (BCLME). *Environmental Development*, *17*, 75–92. https://doi.org/10.1016/j.envdev.2015.07.011

Vichi, M., Lovato, T., Butenschön, M., Tedesco, L., Lazzari, P., Cossarini, G., et al. (2023). The biogeochemical flux model (BFM): Equation description and user manual [Computer software manual]. *Bologna, Italy*. Retrieved from http://bfm-community.eu

Wallschuss, S., Granger, J., Bourbonnais, A., Flynn, R., Burger, J., Pillay, K., & Fawcett, S. (2025). The role of sediments in modulating nitrous oxide production in the southern Benguela Upwelling System: Insights from stable isotopic tracers. *Global Biogeochemical Cycles*, *39*(8), e2024GB008463. https://doi.org/10.1029/2024GB008463

Wanninkhof, R. (2014). Relationship between wind speed and gas exchange over the ocean revisited. *Limnology and Oceanography: Methods*, *12*(6), 351–362. https://doi.org/10.4319/lom.2014.12.351

Weeks, E., Losch, M., & Tziperman, E. (2024). The upwelling source depth distribution and its response to wind stress and stratification. *Journal of Physical Oceanography*, *54*(4), 1003–1018. https://doi.org/10.1175/JPO-D-23-0171.1

Yang, X.-Y., & He, Z. (2014). Decadal change of antarctic intermediate water in the region of Brazil and Malvinas confluence. *Deep Sea Research Part I: Oceanographic Research Papers*, *88*, 1–7. https://doi.org/10.1016/j.dsr.2014.02.007